Journal of Volcanology and Geothermal Research 311 (2016) 198–216

Contents lists available at ScienceDirect

Journal of Volcanology and Geothermal Research

journal homepage: www.elsevier.com/locate/jvolgeores

Review

What can thermal infrared remote sensing of terrestrial volcanoes tell us about processes past and present on Mars?

Michael S. Ramsey [a,*], Andrew J.L. Harris [b], David A. Crown [c]

[a] Department of Geology and Planetary Science, University of Pittsburgh, Pittsburgh, PA, USA
[b] Laboratoire Magmas et Volcans, Université Blaise Pascal, Clermont-Ferrand, France
[c] Planetary Science Institute, 1700 E. Ft. Lowell Rd., Suite 106, Tucson, AZ, USA

ARTICLE INFO

Article history:
Received 24 June 2015
Accepted 15 January 2016
Available online 27 January 2016

Keywords:
Thermal infrared
Volcanism
Lava flows
Discharge rate
ASTER
THEMIS

ABSTRACT

Over the past fifty years, a diverse set of thermal infrared (TIR) remote sensing data has been acquired from the orbits of Earth and Mars, which both have ubiquitous volcanic landforms. These data vary in spatial, spectral and temporal resolution and are critical for investigating an ever-expanding set of science applications including the focus of this review paper: volcanic processes. Volcanic studies using TIR data include active monitoring of flows and plumes on Earth and mapping the compositional and thermophysical diversity on Mars. Furthermore, recent advances in high-resolution, low-cost, ground and laboratory TIR instrumentation now help to augment the orbital data through a synergistic approach to data analysis and validation. Field and laboratory studies also serve as terrestrially-focused analogues that provide important insights to interpret the geologic processes that have operated on other planetary surfaces including Mars. This review expands upon our invited talk of the same title at the 2014 Geological Society of America Meeting to include several case studies designed to give the reader an overview of how TIR data can be applied to volcanic processes on Earth and Mars. These case studies highlight prior work by the authors presented at past meetings, but which have not been published elsewhere. The examples were chosen specifically to identify the TIR data similarities between the two planets, and include analyses of volcanic surfaces to (1) derive composition and texture using TIR spectra (Earth and Mars); (2) analyze mantled flows with thermophysical data (Earth and Mars); (3) estimate lava discharge rate using TIR-derived temperature (Earth with application to Mars); and (4) model flow dynamics based on geomorphic measurements (Mars). Because of our focus on the TIR, we do not attempt to document other remote sensing wavelength regions nor even every volcanic study using TIR data. As TIR instruments have improved over time along similar trajectories, the higher spatial and spectral resolutions provide the ability to examine volcanic processes in more quantitative ways, despite the fact that no TIR instrument has ever been designed solely to study volcanic phenomena. Whether these trends continue for both planets will depend on the design of new TIR technologies, the data they produce, and the science that results from the data.

Contents

* Corresponding author at: Department of Geology and Planetary Science, University of Pittsburgh, 4107 O'Hara Street, Pittsburgh, PA 15260, USA. Tel.: +1 412 624 8772; fax: +1 412 624 3914.
E-mail address: mramsey@pitt.edu (M.S. Ramsey).

http://dx.doi.org/10.1016/j.jvolgeores.2016.01.012
0377-0273/

1. Introduction

The session, *Remote Sensing of Volcanoes in the Solar System*, at the 2014 Geological Society of America Meeting in Vancouver, Canada focused on "advances in the understanding of volcanoes on Earth and other planets enabled by advances in remote sensing technology". Our opening talk was designed both to give an introduction to the remainder of the session as well as to highlight the topic of orbital remote sensing of Martian volcanism with specific attention to terrestrial analog studies that use similar datasets. We chose to further focus on the thermal infrared (TIR) region of the electromagnetic spectrum because of its importance in active volcanic processes on Earth and its prevalence as a data source from satellites in orbit around both planets. For example, Earth-based TIR data have been modeled to derive the eruption rate and progression of active flows, to monitor hazards from active lava domes, and to map the compositional/textural diversity of pyroclastic flows (e.g., Wright et al., 2008; Ramsey et al., 2012a; Krippner and Ramsey, 2013). Near real-time monitoring of the time-averaged discharge rate (TADR) combined with accurate models of the terrain and lava cooling have been applied to predict the flow length with reasonable accuracy (e.g., Favalli et al., 2005; Del Negro et al., 2008). That methodology can be inverted for Mars to infer the eruption conditions responsible for a given flow. TIR data have also been used to derive thermal inertia, a measure of a material's resistance to temperature change (e.g., Palluconi and Kieffer, 1981; Fergason et al., 2006; Price et al., 2013). Such an approach is now being applied to decouple dust/ash mantling from the underlying lava in an attempt to probe its composition, for example (e.g., Ramsey et al., 2012b; Price et al., 2016).

This review paper is a logical extension of the original talk with expanded case studies that now review the similarities and differences both in volcanism and TIR remote sensing data for Earth and Mars. In Section 3, we present case studies that highlight common applications of TIR data to volcanic processes that have occurred on both planets: (1) compositional and textural analysis of lava surfaces; (2) thermophysical response of volcanic terrains; (3) temperature extraction and eruption rate determination; and (4) lava flow propagation modeling. These examples also reflect the expertise and background of the authors.

Even by narrowing the focus to the TIR region, we clearly are not able to review all prior research within such a large topic as the remote sensing of volcanic processes on Earth and Mars. There are obvious omissions in the chosen case studies, such as the detection and quantification of SO_2 and silicate ash in active plumes on Earth (e.g., Watson et al., 2004; Prata, 2009; Prata and Bernardo, 2009); near real-time hot spot detection on Earth (e.g., Dean et al., 1998; Tramutoli, 1998; Wright et al., 2004); the global distribution of igneous/volcanic minerals on Mars (e.g., Bandfield et al., 2000; Hamilton et al., 2003; Koeppen and Hamilton, 2008); chemical alteration of glassy surfaces on Earth and Mars (e.g., Crisp et al., 1990; Kraft et al., 2003; Michalski et al., 2005); and ground-based TIR studies on Earth and Mars (e.g., Christensen et al., 2004; Patrick, 2007; Ramsey and Harris, 2013). Interested readers are directed to the works cited here and the lists of references contained therein for more detail.

2. Background

2.1. TIR remote sensing: Earth/Mars

The TIR region is generally defined as the wavelengths between 5 and 20 μm (2000 and 500 cm^{-1}) for Earth, which is commonly expanded from 5 to 50 μm (2000 to 200 cm^{-1}) for Mars. These regions are nearly entirely available for surface analysis on Mars with the exception of approximately 12.5 to 16.5 μm (800 to 606 cm^{-1}), which is obscured by atmospheric CO_2. In contrast, the larger amounts of H_2O, O_3 and CO_2 in the Earth's atmosphere limit the TIR region to a much narrower range of approximately 8.1–9.3 μm and 10.1–12.2 μm (1235–1075 cm^{-1} and 990–820 cm^{-1}) for surface analysis. The mid-infrared (MIR) region (3 to 5 μm, 3333 to 2000 cm^{-1}) is also available on Earth and commonly preferred for detection of higher temperature lavas. The MIR is also highly sensitive to the presence of sulfates and carbonates, which are of interest for Mars exploration. However, accurate temperature determination and spectral identification in this wavelength region are more difficult as the emitted radiance is particularly sensitive to surface roughness. Furthermore, the surface temperature is much colder and the daytime data have the added complication of contamination by a solar reflected component, both of which lessen the amount of emitted energy reaching the instrument. Although we do show high-spatial resolution image examples of the Earth in the visible/near infrared (VIS–NIR) regions, we do not use these data explicitly for the case study analyses. Similarly, although the SWIR spectral region is used to extract the highest temperatures of lavas found on Earth, which produce maximum emission in this wavelength region following Wein's approximation (Harris, 2013), we do not use it for our case studies in this review, choosing to keep the focus on the TIR region.

2.1.1. Sensors and resolution

For the Earth, TIR data are used primarily for monitoring new and ongoing volcanic activity and subsequent hazard mitigation over young surfaces (e.g., Harris et al., 2002, 2005; Vicari et al., 2009). For such active surfaces, temporal resolution is initially the preference over spectral or spatial resolution in order to support quicker hazard response and mitigation efforts (e.g., Ganci et al., 2011; Gouhier et al., 2011; Vicari et al., 2011). Nearly all sensors in this high temporal resolution class were developed for non-volcanic ground and atmospheric observations and have spatial resolutions greater than 1 km/pixel (Table 1). However, with the increased availability of sensors with improved spatial and spectral resolution in the TIR, new volcanic applications using TIR data have evolved (e.g., Ramsey and Fink, 1999; Vaughan et al., 2005; Ramsey, 2015).

For Mars, compositional and thermophysical mapping is important to enable reconstruction of past event histories (e.g., Christensen, 1986; Bandfield et al., 2000; Rogers and Christensen, 2007). Therefore, improved spectral and spatial resolutions rather than temporal are the primary drivers in sensor development. As with this development trajectory on Earth, Mars sensors have generally improved in spatial and spectral resolution with each new generation (Table 1). For example, repeat orbits to extract the best-data from "pixel stacking" and synergistic use of sensors with high spectral/low spatial and low spectral/high

Table 1
Select list of relevant thermal infrared orbital sensors that have been used for imaging of volcanic surfaces on Earth and Mars. Acronyms here that are not defined in the text include the: Geostationary Operational Environmental Satellite (GOES), Spinning Enhanced Visible and Infrared Imager (SEVIRI), Visible Infrared Imaging Radiometer Suite (VIIRS), Advanced Very High Resolution Radiometer (AVHRR), Infrared Thermal Mapper (IRTM).

	Sensor	Wavelength (μm)	IR spectral channels	Spatial resolution (km)	Temporal resolution
Earth	GOES	10–12	2	4	1 image/15 min
	SEVIRI	8–12	3	3	1 image/15 min
	MODIS/VIIRS	8–12	3	1	1 image/6 h
	AVHRR	10–12	2	1.1	1 image/4–6 h
	TIRS	10–12	2	0.1	1 image/16 d
	ASTER	8–12	5	0.09	1 image/2–16 d
Mars	IRTM	6–30	5	4	n/a
	TES	6–50	143	3	n/a
	THEMIS	6–13	9	0.1	n/a
	Mini-TES	6–50	167	Variable	n/a

spatial resolution generate integrated datasets to allow ever improving understanding of the volcanic history of Mars (e.g., Chicarro et al., 1989; Bandfield et al., 2004; Christensen et al., 2005).

2.1.2. Basic atmospheric considerations

Within the TIR wavelength region, we need to make corrections for the emissive and absorptive properties of the atmosphere as well as surface reflection and scattering at shorter wavelengths (Harris, 2013). Further contamination by gases, aerosols and particles emitted by an active eruptive vent only serves to complicate the situation. This is not a problem encountered on Mars, which neither has active volcanic centers nor thick atmospheric water vapor plumes that hinder surface emitted radiance. However, Mars does have the complications of thin water-ice clouds and silicate dust aerosols. Atmospheric dust on Mars is ubiquitous in the atmosphere and even during periods of the lowest dust loading, the magnitude of its effect on the spectral data is as large as that of any spectral signal from the surface (Conrath, 1975; Smith et al., 2000). Correction of atmospheric emission, absorption and scattering in the TIR is a large issue for both planets, being primarily a gas absorption problem on Earth and an aerosol absorption problem on Mars.

Detection of TIR emitted energy from the surface also known as the "at-surface radiance" is similar for both Earth and Mars. The energy, described by the Plank equation (L(λ,T)) for an isothermal surface, is function of the surface kinetic temperature (T_s), the wavelength of emission (λ) and the wavelength-dependent emissivity (ε_λ) terms:

$$\mathbf{L(\lambda,T)=\varepsilon_\lambda B(\lambda,T_s)=\varepsilon_\lambda\cdot\left\{\left(c_1\cdot\lambda^{-5}\right)/\left(\exp(c_2/\lambda T)-1\right)\right\}} \quad (1)$$

where, $c_1 = 3.74 \times 10^{-16}$ Wm^2 and $c_2 = 0.0144$ mK. The radiance detected by the instrument also known as the "at-sensor radiance" is the at-surface radiance modified by the emission/scattering from the atmosphere, which can complicate extraction of accurate surface temperature and/or emissivity (Harris, 2013). Regardless of the planet, the atmosphere imparts indirect and direct effects, including the wavelength-dependent transmission ($\tau_\lambda(\theta)$), the down-welling radiance emitted by the atmosphere and reflected by the surface ($L_i^{\downarrow}$) and up-welling radiance emitted by the atmosphere directly to the sensor ($L_\lambda^{\uparrow}$):

$$\mathbf{L_\lambda(\theta)=\tau_\lambda(\theta)\cdot[\varepsilon_\lambda B(\lambda,T_s)+\tau_\lambda(\theta)]\cdot(1-\varepsilon_\lambda)\,L_i^{\downarrow}+L_\lambda^{\uparrow}} \quad (2)$$

The down-welling and up-welling terms can generally be assumed to be blackbody in nature (ε = 1.0 at all wavelengths), and for a cold atmosphere (compared to a warmer surface), these terms are negligible. This generally would be the case for Mars, although atmospheric emission is an explicit constant that is removed during atmospheric correction. On Earth, however, which has a warmer atmosphere and surfaces with deeper emissivity features, the down-welling energy, which has the effect of muting the depth of the surface spectrum, can be a significant component of the at-sensor radiance. Within the generally "clear" atmospheric windows, the transmission term is also commonly assumed to be close to or at 1.0. This assumption can fail, however, on Mars where silicate dust obscures the surface and thereby lowers $\tau_\lambda(\theta)$. Therefore, some assumption or *apriori* knowledge of the atmosphere at the time of data acquisition is critical for accurate surface measurements, particularly in the case of low-temperature surfaces where the atmosphere contributes a proportionally larger effect.

2.1.3. Surface emission

The penetration depth of the at-surface TIR radiance from any planetary surface is only sensitive to the uppermost surface layer, varying from approximately 10 to 100 μm for spectroscopy to decimeters for thermophysical analysis. This emitted radiance at temperatures above 0 K (−273 °C) is described by the Planck equation (Eq. (1)). The total energy increases with surface temperature and the wavelength of the peak emission shifts to shorter wavelengths with this increase. This shift is approximated by Wien's displacement law:

$$\lambda_m = \mathbf{2898\ \mu m\ K/T(K)} \quad (3)$$

in which λ_m is the wavelength of peak emission and T is the temperature of the surface in K. Having the capability to detect emission near the peak wavelength region is especially important where observing thermally-mixed pixels containing some fraction of hot material with the remainder being at the background temperature. Accurate separation of these fractions at widely-varying temperatures is much easier in the wavelength region where the Planck curve is rapidly changing (i.e., near the peak emission). For example, a surface at 1273 K (1000 °C) and one at 298 K (25 °C) will both have generally flat Planck curves in the TIR region; meaning that a mixture of the two will produce a similarly flat curve, which makes thermal deconvolution problematic. On Earth, active volcanic systems can have temperatures that range from approximately 373 K (100 °C,) (e.g., fumaroles) through 1473 K (1200 °C) (e.g., molten lava), so that λ_m ranges between 7.8 and 2.0 μm (see Harris, 2013). For Mars, where surface temperatures range between approximately 133 K (−140 °C) and 308 K (35 °C) (see Table 2), λ_m ranges between 9.4 and 22 μm. Therefore, detectors that

Table 2
Planet-scale parameters for Mars.

Distance from the sun	1.52 AU
Day length	1.03 Earth days
Year length	1.88 Earth years
Mass	6.4×10^{20} kg
Density	3.9 g/cm^3
Radius	3390 km (0.55 times Earth)
Surface temperature	130–308 K
Gravity	3.8 m/s^2 (0.38 times Earth)
Surface pressure	0.07 bar

operate solely in the TIR wavelength region are more common for Mars. For Earth, although the average surface temperatures result in peak emission in the TIR region, detection of the maximum emission from active volcanic surfaces commonly requires detectors in the MIR and SWIR regions (see Electronic Supplement 1 of Harris, 2013). The surface radiance in these regions can therefore also contain a solar reflected component that complicates accurate analyses for daytime scenes. As we move into the TIR, this reflectance term declines, making it more straight-forward to retrieve surface brightness temperature at any time of the day. Despite these differences, data in the TIR region are being acquired for both planets and have been beneficial for studies of active, cooling and older lavas on Earth (e.g., Harris, 2013) as well as the volcanic surfaces of Mars (e.g., Christensen et al., 2005; Edwards et al., 2008).

2.1.4. Emissivity

A surface is considered an ideal radiator (i.e., blackbody) if it absorbs completely and reemits all input radiation in the wavelength region under consideration. However, nearly all natural materials and surfaces do not behave as blackbodies, having predictable wavelength-dependent variability in their emission spectra (Fig. 1). To describe this variability, the Planck equation is modified by the wavelength-

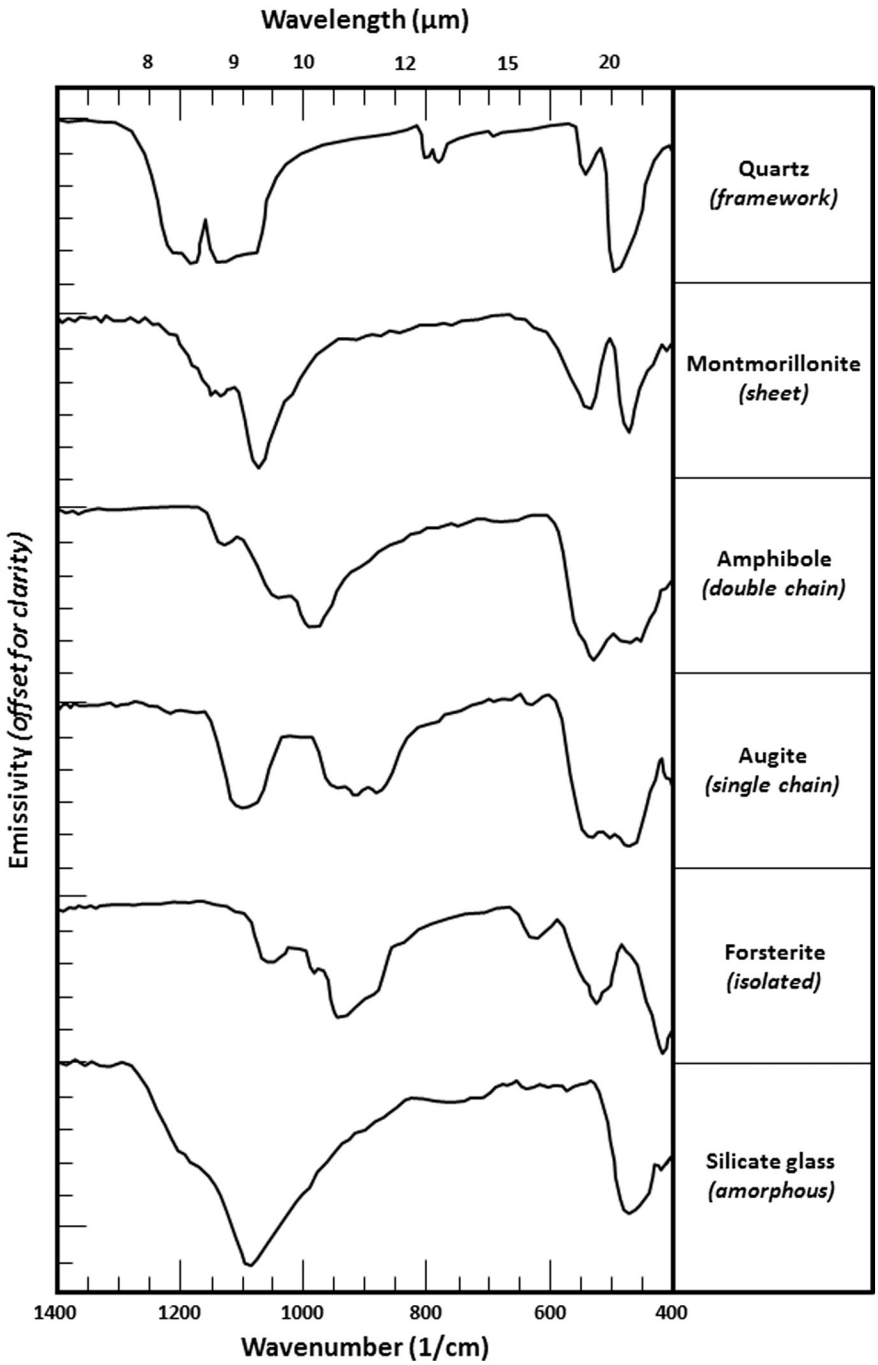

Fig. 1. Emissivity spectra of several common silicate minerals representing the different silicate classes and their structural order. The spectra (and to some degree the spectral classes) are distinguished by the position and morphology of the primary emissivity feature in the 8–12 µm (1250–833 cm^{-1}) region. These spectra are chosen to show a range of common minerals rather than those most common in igneous rocks on either Earth or Mars. Note the relative lack of narrow-band features in the amorphous high-silica glass spectrum compared to the crystalline minerals. Spectra are resampled to 4 cm^{-1} (from 2 cm^{-1}) to reduce high-frequency noise not related to the mineralogy. Each vertical tick mark represents 0.1 emissivity units and no normalization has been performed on the spectra.

dependent emissivity term, $\varepsilon(\lambda)$. In its simplest form, the emissivity is the ratio between the measured spectral radiance ($L(\lambda,T)$) at a given wavelength to that of the blackbody radiance ($L_{BB}(\lambda,T)$) at the same temperature and wavelength:

$$\boldsymbol{\varepsilon}(\boldsymbol{\lambda}) = \mathbf{L}(\boldsymbol{\lambda}, \mathbf{T})/\mathbf{L}_{\mathbf{BB}}(\boldsymbol{\lambda}, \mathbf{T}) \quad (4)$$

On Earth and Mars most surfaces either behave as grey bodies (a constant emissivity less than 1.0) or selective radiators (emissivity varies with wavelength). Earth-based studies have shown that emissivity varies predictably with surface composition, lava vesicularity, degree of crystallinity and the micron-scale surface roughness (e.g., Salisbury and D'Aria, 1992; Ramsey and Fink, 1999; Byrnes et al., 2004; Carter et al., 2009). Furthermore, an emitting surface comprised of fine-grained particles can also affect the emissivity due to scattering and diffraction effects (Moersch and Christensen, 1995; Ramsey and Christensen, 1998; Hapke, 2012). Emissivity variations for coarser-grained surfaces are due primarily to either surface roughness or compositional variability. TIR data show that uniform temperature, low albedo volcanic surfaces on Mars are dominantly basalt (Bandfield, 2009; Ramsey and Crown, 2010). Most low-albedo regions on Mars are rarely bedrock, however, with thermal inertia revealing that many are mantled with a silt to sand sized regolith (e.g., Fergason et al., 2006; Rogers and Christensen, 2007). The dominant exception are surfaces that lie in high-albedo (brighter) regions and are therefore covered by some amount of fine-grained air fall dust or eolian mantling. These bright regions are estimated to have millimeters to meters of dust, which results in a blackbody emitting surface due to the scattering of the fine-grained dust particles (Christensen, 1986; Ramsey and Christensen, 1998; Johnson et al., 2002). Therefore, these regions are commonly excluded in TIR compositional studies of the martian surface. One could argue that from the TIR perspective, clouds, water bodies and vegetation have a similar masking effect on Earth.

2.2. Volcanism: Earth versus Mars

Volcanism has been a primary geologic process on both Earth and Mars throughout their geologic histories. Similarities as well as fundamental differences in the styles, scale, composition, and tectonic controls have been recognized (e.g., Keszthelyi et al., 2000). The most common composition for both planets is basalt, although Earth has a much greater compositional variety in its erupted products. The implication is that there is a prevalence of relatively low viscosity lava on Mars relative to the wider range of lava types and rheologies observed on Earth. There are clear exceptions to this commonality and we highlight some of those in the subsequent case studies. However, the volume of erupted lava over their histories makes both Earth and Mars basaltic planets in a general sense. One of the obvious differences is the current presence of active volcanism on Earth as compared to Mars. Therefore, the toolkit of techniques developed for TIR remote sensing on Earth has evolved to include an emphasis on high-temperature studies, active lava flow modeling, and hot-spot detection. On Mars, the techniques focus more on compositional and thermophysical differentiation of igneous surfaces, particularly in the low-albedo regions of the planet (e.g., Rogers and Christensen, 2007; Koeppen and Hamilton, 2008; Edwards et al., 2008).

The history of terrestrial TIR data analysis and diversity of terrestrial volcanism provide a foundation to interpret volcanic processes that have operated on Mars in the past. Models developed to derive composition or the flux rate of active lava flows on Earth can be adapted for older, solidified flows on Mars, for example. We discuss basic similarities and differences in volcanism between Earth and Mars in the following sections. We also refer the reader to a number of useful treatments of volcanism on Mars that have been compiled over the years and updated as new spacecraft observations were acquired. These include catalogues of Martian volcanic features and consideration of Martian eruption processes (Carr, 1973; Greeley and Spudis, 1981; Mouginis-Mark et al., 1992; Hodges and Moore, 1994; Wilson and Head, 1994; Greeley et al., 2000; Plescia, 2004; Zimbelman et al., 2015). In addition, the series of datasets that have provided extensive aerial coverage of the Martian surface have allowed geologic maps to be produced of volcanic landforms at various scales and document their morphologic characteristics, relationships to the surrounding landscape, and stratigraphic and chronologic constraints (see Greeley, 2007 for review). Recent and ongoing analyses in this area have relied predominantly on the Thermal Emission Imaging System (THEMIS) TIR mosaic for global, regional, and local studies, which is yet another use of TIR data (e.g., Crown and Greeley, 2007; Platz and Michael, 2011; Bleacher et al., 2013; Garry et al., 2014; Tanaka et al., 2014; Crown, 2015; Gregg et al., 2015).

2.2.1. Volcanic similarities: Earth versus Mars

Mars exhibits an array of extrusive volcanic features similar to that of the Earth, and their formation processes have been interpreted based on morphology and the modeled eruption conditions that formed these morphologies (Fig. 2). Volcanic landforms on Mars include lava flows/fields, lava channels/tubes, flood basalts, volcanic craters, cinder cones, shields, calderas, dikes, and pyroclastic deposits for which Earth-analogs abound (e.g., Keszthelyi et al., 2000; Mouginis-Mark et al., 2007). There is also evidence for lava-ice and lava-water interactions on Mars, generating features for which terrestrial examples such as rootless cones/pseudocraters, tuyas, and lava deltas are found (e.g., Fagents et al., 2002; Skilling, 2002; Hamilton et al., 2010). Mars is similar to Earth in density, composition, formation processes and surface modifications (Greeley, 2007). Therefore, one would expect similar processes and styles of volcanism (Carr et al., 1980; McGetchin et al., 1981). Key properties of Mars as a whole, especially those important for processing and modeling thermal infrared data are given in Table 2.

2.2.2. Volcanic differences: Earth versus Mars

Despite their similarities in some respects, there are also some major differences in volcanism on Mars and Earth. From the earliest days of Mars exploration, the volcanic products were observed to be orders of magnitude larger than common analogs on Earth (Carr et al., 1980; McGetchin et al., 1981; Cattermole, 1996; Frankel, 1996; Greeley, 2007). For example, Martian lava flows are up to 500 km long and summit calderas have dimensions of 80 × 65 km by 2.5 km deep. The scale differences also lead to proposed eruption rates that are many orders of magnitude larger than those encountered on Earth (e.g., Crisp and Baloga, 1990). Regardless, higher volumes of magma were stored in, and withdrawn from, Martian shields in comparison to Earth shield volcanoes. The enormous shield volcanoes are the most prominent volcanic landforms on Mars and seem to, along with extensive flow fields and volcanic plains, dominate the volcanic history of the planet (Greeley, 2007). Large scale explosive volcanism also may have played a significant role early in Martian history, creating the expansive, low-relief highland paterae and also perhaps accumulating to form the Medusae Fossae Formation (e.g., Scott and Tanaka, 1982; Greeley and Crown, 1990; Crown and Greeley, 1993; Mandt et al., 2008). Bandfield et al. (2013) used morphological and thermophysical properties along with comparisons to other planetary analogs to conclude that most of the older surfaces on Mars are dominated by fine-grained material (sand and smaller particle sizes) that are weakly indurated. The younger surfaces, on the other hand, appear to be dominated by blocky lava flows with higher thermal inertia. A logical hypothesis offered for this disparity is that of an early wet mantle that eventually became volatile-depleted without replenishment from plate tectonic activity.

The second fundamental difference between the two planets is the presence of active plate tectonics on Earth. It results in a planet-wide distribution of volcanic centers with volcanism located around plate boundaries and at static hot spots. Furthermore, motion of the plates over the static hot spots commonly results in chains of low-profile

basaltic shields, such as the Hawaiian-Emperor chain or large outpourings of flood basalts throughout Earth's history. The same tectonic processes also lead to a much larger compositional diversity on the Earth, with basalt dominating hot spot and spreading center volcanism, whereas more evolved lavas (i.e., andesites, dacites and rhyolites) are common at subduction zones and island arc settings (McGetchin et al., 1981; Francis and Wood, 1982).

No conclusive signs of plate boundaries or subduction are found on Mars, suggesting neither plate motions nor plate tectonics in the strictest sense (McGetchin et al., 1981). TIR data from the Thermal Emission Spectrometer (TES) instrument did differentiate compositions between the northern lowlands and southern highlands, with the former closer to the bulk composition of andesite and the latter to that of basalt; however, no tectono-volcanic origin was implied. Later TIR studies suggested that the higher-silica terrane may be the result of chemical aqueous alteration that produced a silica-rich alteration product (e.g., Wyatt and McSween, 2002; Michalski et al., 2005). More recent TIR studies have shown there are at least nine different globally abundant compositions, some of which can only be understood as resulting from variations in original mineralogy (e.g., Rogers et al., 2007; Rogers and Hamilton, 2015). Rather than the tectonic-influenced volcanism on Earth, hot spot volcanism above mantle plumes below a static crust dominated Mars in the past, along with volcanism in response to lithospheric fracturing and impact events (McGetchin et al., 1981). The lack of plate tectonics results in a relative compositional homogeneity across the surface Mars. However, smaller-scale igneous compositional diversity has been noted mainly through analysis of data from the various Mars rover missions. Rieder et al. (1997), for example, found that the soil at the Pathfinder landing site was more similar to terrestrial andesites (Table 3), whereas McSween et al. (2006) used thermal emission

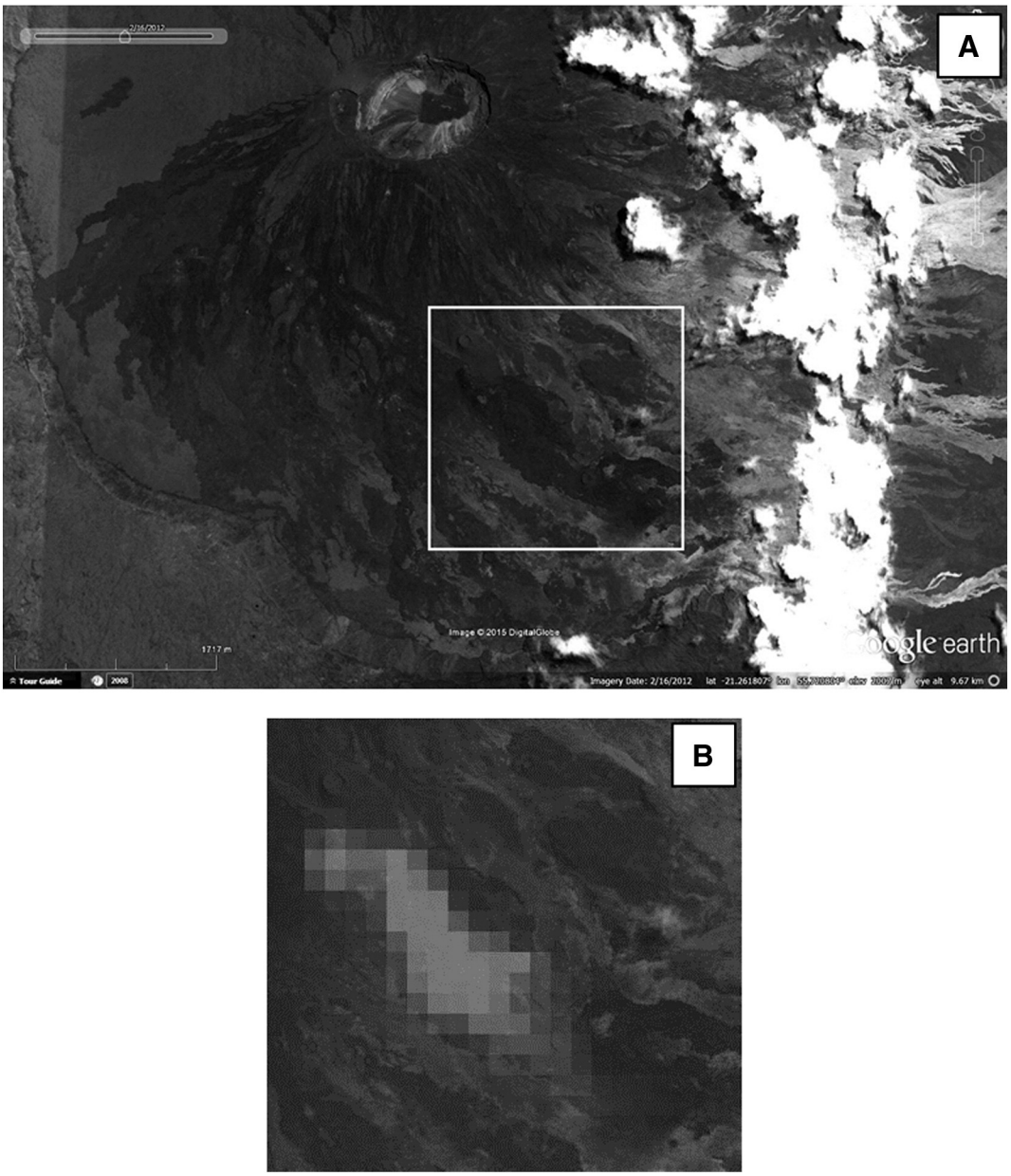

Fig. 2. Comparison of "typical" basaltic lava flows on Earth and Mars. (A) Digital Globe image acquired on 16 Feb. 2012 of Piton de la Fournaise volcano on Reunion Island. Image was archived in Google Earth and modified to show the lava flow formed during the 14 Oct. 2010 eruption (white box). The box also indicates the area shown in (B). (B) ASTER night time TIR data acquired on 19 Oct. 2010 overlain on the Digital Globe image for context. Each TIR pixel is 90 m. (C) Context (CTX) Camera visible image (Image ID D09_030863_1574_XN_22S116W) centered at 243.27E, 22.42S showing two relatively unmodified (higher albedo) flows in the Arsia Mons southern flow field. (D) Same image as (C) overlain by the THEMIS day IR 100 m (v. 12) global mosaic (Edwards et al., 2011). The daytime IR pixels of the flows are cooler (i.e., higher thermal inertia) than the surrounding lava plains and therefore presumed to be less mantled by lower thermal inertia airfall dust (i.e., younger in exposure age).

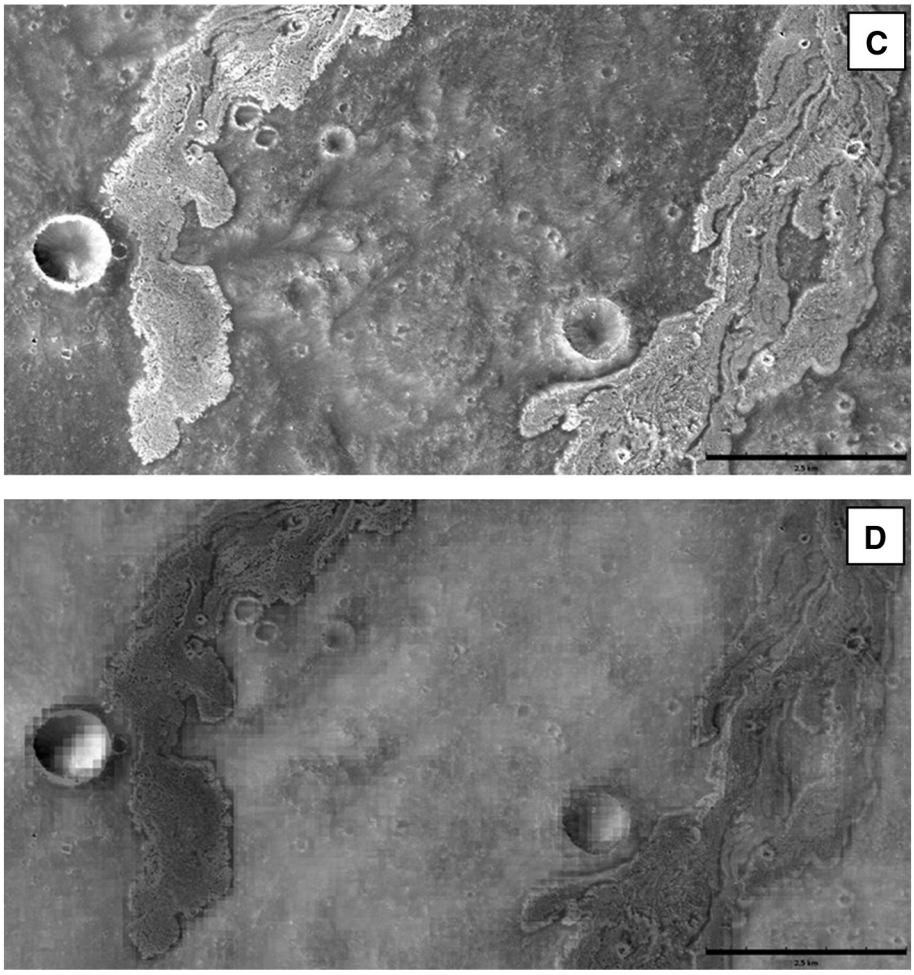

Fig. 2 (*continued*).

spectra from the Mars Exploration Rover to identify three classes of alkaline igneous rocks in the Columbia Hills of Gusev crater. Hamilton et al. (2003) compared TES-derived surface compositions with TIR data of martian meteorites and found few matches. These results are perhaps not surprising as nearly all martian meteorites are extremely young relative to most of the non-dust mantled surfaces on Mars. However, Lang et al. (2009) showed that the thermal infrared spectral signatures of lava flows in Daedalia Planum with low dust cover were consistent with those of SNC meteorites, particularly basaltic shergottites. Later orbital TIR data from both the TES and THEMIS instruments found very sparse evidence of either ultramafic lavas or more evolved, silica-rich lavas (e.g., Christensen et al., 2005). The high-silica compositions identified by the Pathfinder and Mars Exploration Rovers are consistent with those identified by TES. Similarly, MSL has been identifying what is being interpreted as more evolved compositions that appear to be consistent with the magmatic diversity identified by Christensen et al., 2005. An ongoing debate continues as to whether these represent alteration or are derived from original primary volcanic compositions.

Table 3
Compositional comparison of one in-situ measurement from the Mars Pathfinder X-ray spectrometer in July–August 1997 (Rieder et al., 1997) to that of a Martian meteorite (Zagami).

	Zagami Meteorite (wt.%)	In-situ sample A3 (wt.%)
SiO_2	49.6	58.6 ± 2.9
TiO_2	1.0	0.8 ± 0.2
Al_2O_3	7.1	10.8 ± 0.1
FeO	17.4	12.9 ± 1.3
MgO	8.8	3.0 ± 0.5
CaO	10.9	5.3 ± 0.8
Na_2O	2.3	3.2 ± 1.3
K_2O	0.25	0.7 ± 0.1

Plate motion on Earth (or the lack thereof on Mars) also results in size differences between similar volcanic constructs. Earth's plate motions continually carry shields away from their sources and results in many small, coalesced shields to form, rather than a few, isolated, larger shields seen on Mars. Persistent effusion of low-viscosity basalt at single sites due to the lack of plate motion on Mars has led to the construction of enormous shields over hundreds of millions of years. The low viscosity of the lava resulted in low angle shield formation (e.g., Olympus Mons), with typical slopes similar to those encountered at terrestrial basaltic shields; however the scale of these structures is much larger (Fig. 3). The age of Olympus Mons ranges from ~100 million years (Mya) to ~3.8 billion years (Gya) (Werner, 2005), during which almost 4.0×10^6 cubic kilometers of basalt were erupted. It is a single, isolated shield with a typical slope of 4° but a basal diameter of 600 km and a height (above the Mars datum) of 27 km, which is 100 times the volume of Mauna Loa. Even if Mauna Loa erupted at a time-averaged rate of 1.1×10^{-3} km^3 per year at the same location over 115 million years, a volume of only 0.12×10^6 km^3 would be produced; meaning that magma production rates at Olympus Mons were also consistently higher than at Mauna Loa (Wilson and Head, 1994).

Mars also has a series of volcanic constructs that are different from anything similar seen on Earth. For example, dome volcanoes or tholi,

Fig. 3. Comparison of Olympus Mons with the country of France. © *Sémhur/Wikimedia Commons/CC-BY-SA-3.0.*

which are smaller and steeper than Martian shields, are likely comprised of lavas mixed with pyroclastics and are possibly the result of eruption of more viscous lavas at lower discharge rates (Greeley, 2007) although no compositional confirmation of this assumption has been found due mainly to the fact that these constructs occur in dusty regions where TIR cannot detect the bedrock composition. They are less common than volcanic domes on Earth, due to the lower silica content of the lava; but also much larger with shallower slopes. Ceraunius Tholus, for example, has a slope of 7°, but dimensions of 130 × 92 km, a summit caldera 23 km in width and a 2 km wide lava channel that descends from the caldera to the base. The high viscosities and associated constructional features of more evolved lavas found on Earth rarely occur on Mars (Christensen et al., 2005).

3. Case studies

3.1. Compositional/textural analysis

All major rock-forming minerals common to the range of volcanic rocks found on Earth and Mars have diagnostic spectral features in the TIR region (Fig. 1). In the most general sense, the dominant emissivity minimum in the 8–12 μm region shifts from shorter to longer wavelength with decreasing silica polymerization (Lyon, 1965; Hunt, 1980; Salisbury and Walter, 1989). For example, the emissivity low of a framework silicate like quartz occurs between approximately 7.5 and 9.3 μm (1333 and 1075 cm^{-1}), whereas that of an isolated silicate like forsterite appears between approximately 10.2 and 11.7 μm (980 and 855 cm^{-1}). This change with wavelength allows discrimination of felsic and mafic lava surfaces using relatively simple band differencing or a slightly more complex decorrelation stretch (DCS) approach using three of the TIR wavelength channels (e.g., Gillespie, 1992). These detection techniques are ideal for rapid surveys of new lava surfaces on Earth (e.g., Kahle et al., 1988; Buongiorno et al., 2002; Byrnes et al., 2004) or scanning larger areas on Mars in a search for petrological variations (e.g., Bandfield et al., 2004; Osterloo et al., 2008). However, more detailed analyses are possible by examining individual pixel-integrated emissivity spectra. Depending on the spectral resolution of the TIR instrument, such an analysis can produce information on the type and percentage of specific mineral assemblages, as well as the degree of vitrification and surface vesicularity, all of which directly affect the TIR spectrum. Clearly, higher spectral resolution data allow for more subtle spectral features to be discriminated, whereas multispectral data can typically only resolve broad mineral classes at best.

Important considerations for examining TIR spectral data of lava flows and igneous materials are the degree of vitrification and surface micron-scale roughness present (e.g., Byrnes et al., 2004). All extrusive lava contains some degree of glass whether as surface coatings common on basaltic pahoehoe flows or interstitially between larger crystalline phenocrysts in some high-silica lava domes. The presence of this glass results in a TIR spectrum with a broad silicate absorption that lacks

narrow (and more diagnostic) spectral features (Fig. 1) and whose emissivity minimum varies only slightly in wavelength position with composition compared to their crystalline counterparts (e.g., Minitti and Hamilton, 2010; King et al., 2011). This can make it difficult to extract more detailed information on the lava composition using TIR data. The spectral feature of glass is also similar to that of other amorphous materials, which can lead to confusion (Kraft et al., 2003; Michalski et al., 2005). Furthermore, glassy surfaces (especially on Earth) can alter rapidly due to chemical weathering. For example, Kahle et al. (1988) found that TIR spectra of some Hawaiian basalt flows indicated much higher silica content than nearby flows. They used these differences to map the relative ages of the flows, with older flows appearing more silica-rich. A more detailed investigation of the spectra of samples from these flows by Crisp et al. (1990) revealed that the glassy surfaces were being chemically-altered and opalized over time with prolonged exposure to the acidic environment. Kahle et al. (1988) also found that the rougher surfaces of a'a flows had less-distinct spectra that tended more toward that of a blackbody. They termed this scattering phenomenon 'cavity radiation', and postulated that it was produced by multiple scatterings and reflections of the emitted TIR photon by the rough surface. Later work by Ramsey and Fink (1999) and Carter et al. (2009) quantified this process noting there was a linear relationship between the degree of micron-scale surface roughness and the reduction in spectral contrast of the glassy spectral feature. This allowed the surface vesicularity to be extracted for each pixel to within 5% accuracy. The linear relationship between the areal amount of a mineral, surface coating or vesicularity and the morphology of the spectral feature has been noted by several past studies and makes TIR spectral analysis a powerful and straight-forward analytical tool. With a known spectral library of minerals or glasses for example, spectra of volcanic surfaces imaged by TIR remote sensing data can be deconvolved to not only model specific minerals or the surface vesicularity but also the percentage of each component within a given pixel (e.g., Thomson and Salisbury, 1993; Ramsey and Christensen, 1998; Koeppen and Hamilton, 2008; Rogers and Aharonson, 2008).

The linear deconvolution modeling approach for TIR spectra has been used on numerous occasions for analysis of TIR data for Earth and Mars. One such example was the work of Ramsey et al. (2012a) who used TIR data from the Advanced Spaceborne Thermal Emission and Reflection Radiometer (ASTER) instrument to analyze the deposits following the large 2005 eruption of Shiveluch volcano on the Kamchatka Peninsula, Russia. The 27 February 2005 explosive eruption produced a pyroclastic flow deposit (PFD) approximately 24,800 m^2 in size. This PDF travelled 11.5 km to the southwest and another 7.5 km to the west before terminating (BGVN, 2005). A field investigation of the deposit three days later revealed that the PFD was dominated by pumice as well as large blocks from the old dome that had travelled over 10 km from the summit. Ramsey (2012) focused on mapping the surface temperature and vesicularity of this deposit using ASTER TIR data in the months following the eruption. The first image was acquired on 12 March 2005 with new images following approximately every week for the next several months. The entire deposit was found to be approximately 283 K (10 °C) above the average background temperature on 12 March with smaller areas on the PFD exceeding pixel-integrated temperatures of over 343 K (70 °C). By 29 March, the deposit had cooled significantly with approximately 50% of the deposit (mainly in the most distal portion) remaining elevated by 283 K (10 °C) above the background. The same data modeled for vesicularity also showed significant changes during this time period (Fig. 4). The 12 March TIR data had an average vesicularity of 55%, which decreased to 45–50% in the central portion of the distal deposit. Interestingly, this region was found to contain most of the larger dome blocks, whereas the rest of the PFD was dominated by fine-grained ash and pumice from the column collapse. The TIR data from 29 March showed a significant decrease in the modeled surface vesicularity. The average value was now 45%, with areas of the deposit found to be as low as 30%. This trend continued over the next five months albeit at a much slower rate. In August, a field campaign was conducted and the deposit examined in detail. It was found to be mostly devoid of loose pumice on the surface, which had become well-indurated and incised in areas by water (Ramsey, 2012). The patterns in the TIR data revealed a surface that was being modified over time by eolian and fluvial activity rather than having a volcanological cause. However, Ramsey (2015) was able to use this same approach to link surface vesicularity in pyroclastic flow deposits to their specific formation mechanism (e.g., column versus dome collapse).

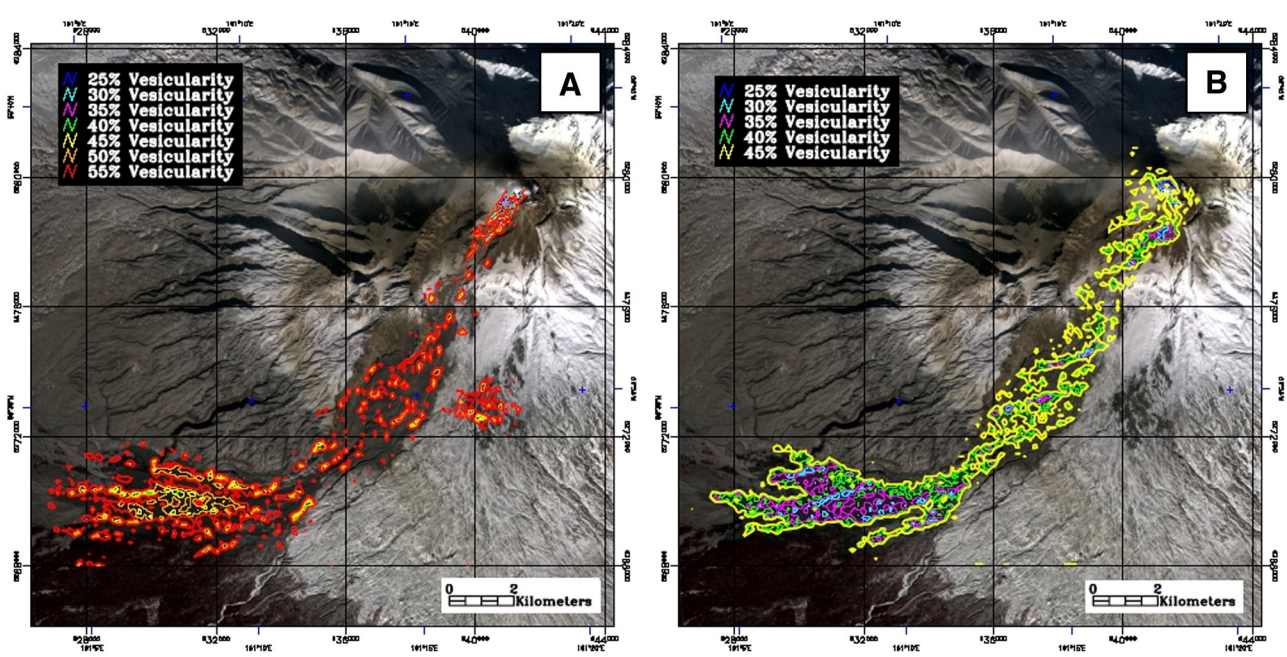

Fig. 4. Modeled surface vesicularity of the 27 February 2005 pyroclastic flow deposit (PFD) on Shiveluch volcano, Russia (Ramsey, 2012). A deconvolution approach using library spectra of glass and a blackbody was applied to the ASTER TIR data in order to map the percent vesicularity of each pixel on the PFD. The results were contoured and draped on the ASTER visible/near infrared image acquired on 12 March 2005. North is up in both images. (A) 12 March 2005. (B) 27 March 2005.

A similar approach to deconvolving TIR spectra was performed by Christensen et al. (2005) in order to resolve a high-silica mineral assemblage in a lava flow located in the caldera of the Syrtis Major shield on Mars. An initial survey of THEMIS nighttime data revealed that portions of the Nili Patera summit caldera had higher TIR temperatures than the surrounding surfaces indicating the presence of a high thermal inertia unit (see Section 3.2), which was postulated to be bedrock swept free of dust and sand by active winds and the presence of barchan dunes. A decorrelation stretch of three of the THEMIS channels discriminated basalt as well as a higher silica flow unit (Fig. 5). With multispectral TIR data, this level of unit differentiation is commonly all that is possible. However, Christensen et al. (2005) also had access to data from the TES instrument, a prior hyperspectral orbital TIR sensor. TES data from both units in the caldera looked distinctly different and were deconvolved using a spectral library of minerals and the approach of Ramsey and Christensen (1998). The results showed that the two units were in fact different rock types (Fig. 5). The majority of the surface units had a distinct basaltic spectrum with plagioclase and clinopyroxene comprising 60% of the unit based on the deconvolution results. However, the other flow unit was dominantly plagioclase plus high-silica glass (65% of the total detected) with a calculated SiO_2 abundance of 60–63 wt.%. Based on these compositional results, the authors conclude that this unit is most similar to dacite lava flows on Earth and likely originated from evolution within the magma chamber below Nili Patera at some time later than the eruption of the earlier low-silica basalt flows.

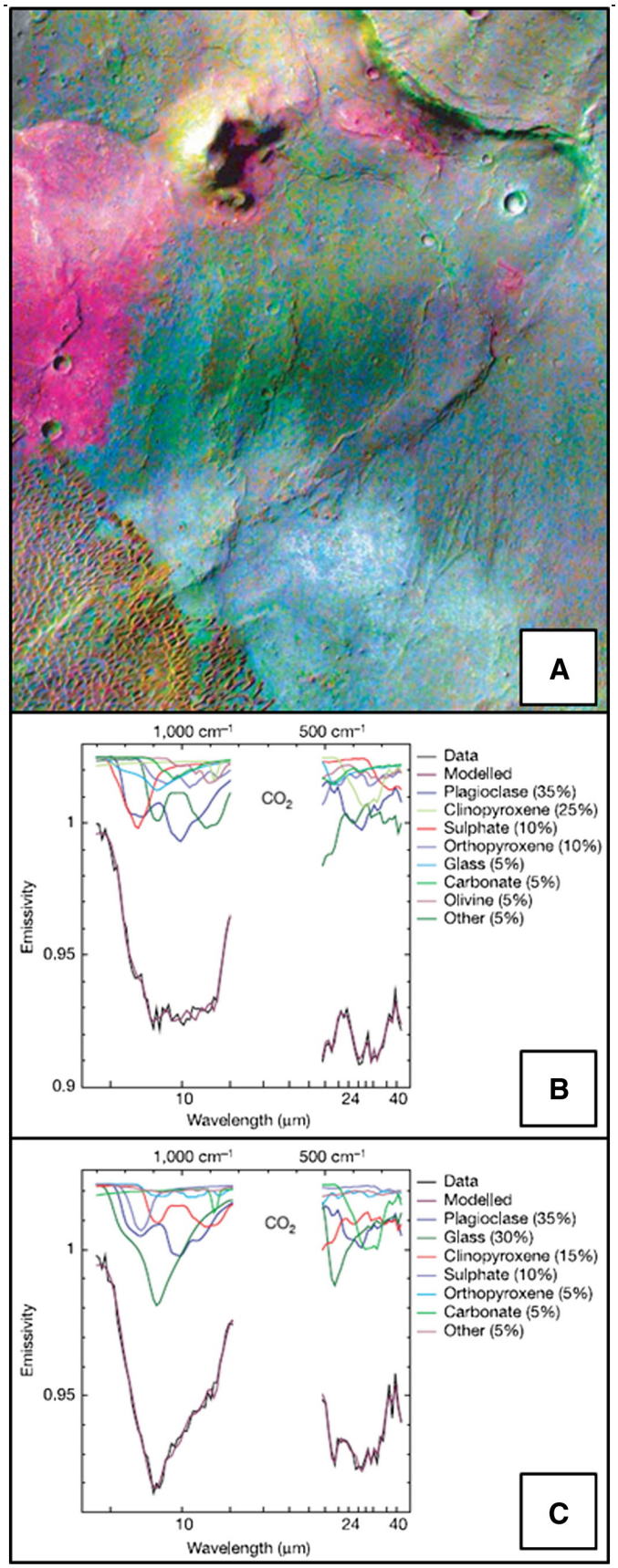

Fig. 5. Figure modified from Christensen et al. (2005) showing their TIR compositional analysis of Nili Patera. (A) Spectral decorrelation stretch of the 100 m/pixel THEMIS data with TIR bands 9, 7 and 5 in red, green and blue respectively. In this color composite, basalt surfaces are blue to cyan whereas the more silica-rich dacite flow is magenta. The TIR data are overlain on a THEMIS visible image at 18 m/pixel for context. (B) Spectral deconvolution result for the basalt surface. (C) Spectral deconvolution result for the dacite surface. The end-member results are rounded to the nearest 5% and their spectra scaled at the top of each figure on the basis of their derived abundances.

3.2. Thermophysical variability

In the broadest sense, thermophysical variability refers to the distinction of surface temperatures based on diurnal and seasonal energy cycles, albedo, and phase behavior. Thermal inertia is the specific parameter that defines the resistance of a material to a time-varying change in temperature (Kieffer et al., 1977; Price, 1977). Specifically, it is defined as:

$$\mathbf{I}=(\mathbf{K}\rho\mathbf{c})^{1/2} \tag{5}$$

where, **K** is the thermal conductivity, **ρ** is the density, and **c** is the specific heat. The thermal inertia of a planetary surface is affected by a wide variety of factors including particle size, the presence of cementing agents, soil moisture, ice, and local slopes to name a few. Furthermore, it is sensitive to the thermal skin depth of the surface and therefore commonly probes much deeper than spectral- or temperature-dominated emission from the uppermost surface.

Because Martian surfaces have apparent time-varying thermal inertia due to a complex interplay of heterogeneous surfaces below the scale of the pixel the phrase "apparent thermal inertia" (ATI) has been used (e.g., Putzig and Mellon, 2007). This is in contrast to the terrestrial literature, where ATI is a quantitative approximation of thermal inertia derived from satellite-based measurements and defined as:

$$\mathbf{ATI}=\mathbf{nc}\,(\mathbf{1}-\mathbf{a})/\Delta\mathbf{T} \tag{6}$$

where, **a:** VNIR albedo; **ΔT**: day/night temperature difference; **n** and **c**: scaling factors for solar flux variability and solar declination with latitude. Therefore, ATI is a relative measure of the absorbed solar radiation (i.e., 1 − albedo) to the diurnal temperature change (Price, 1977; Kahle, 1987; Scheidt et al., 2010). Both thermal inertia and apparent thermal inertia provide us with yet another application for TIR data.

Quantitative thermal inertia has a long history in the study of the geology of Mars, whereas the quantitative ATI approximation is used more widely in terrestrial studies. The thin atmosphere of Mars with its low

amounts of water vapor and the lack of precipitation allow for more straight-forward thermal modeling of the surface, which can be used to relate surface temperature directly to thermal inertia (e.g., Kieffer et al., 1977; Palluconi and Kieffer, 1981). In contrast, the thicker and wetter atmosphere of Earth makes this modeling of grain to grain heat transfer on the surface a more difficult proposition. Thermal inertia investigations of Earth also have to account for vegetative cover and variable soil moisture. ATI, therefore, was developed as a proxy for thermal inertia, being used for a wide variety of applications including derivation of soil moisture, water resources and agricultural mapping (e.g., Rosema and Fiselier, 1990; Cai et al., 2007; Scheidt et al., 2010).

More recent studies have examined the application of thermal inertia and ATI to volcanic questions on Earth and Mars, specifically focused on the presence of mantling deposits over primary flow features (Peet et al., 2007; Ramsey and Crown, 2010; Price et al., 2013, 2016). For example, Arsia Mons is the southernmost of the Tharsis shield volcanoes on Mars and has two large lava flow aprons that extend from alcoves on the NE and SW flanks (Plescia, 2004). The SW apron has an extensive flow field with individual flows exhibiting a wide range of morphologies, surface textures, degrees of eolian mantling, and unusual thermophysical characteristics (Bandfield, 2009; Ramsey and Crown, 2011; Crown, 2015; Crown et al., 2015; Price et al., 2016). Some of these flows show no temperature change at all between the day and night TIR data, which is quite unusual for either a blocky, unmantled flow or a heavily mantled flow (Fig. 6). This lack of a temperature change is likely the result of an albedo-dominated influence of radiant temperature in the daytime data plus the presence of some amount of surface dust (Ramsey and Crown, 2010; Ramsey et al., 2012b; Simurda et al., 2015). However, this is not a uniform regional process because adjacent flows can have a distinct temperature change from day to night. This change from cooler in the day to warmer at night indicates the presence of blockier, less-mantled surfaces. The observed variability in thermophysical behavior across this flow field coupled with extensive areal coverage by high resolution visible wavelength images suggests that future quantitative analyses of the TIR data will provide important constraints on not only volcanic processes but on the degradation of individual flow surfaces.

Mantled lava flows also exist on Earth with one well-studied example being the Mono Craters and Domes (MCD), an arcuate chain of high-silica lava flows in east-central California that formed over the past 10,000 years (Bursik and Sieh, 1989; Hildreth, 2004). An ASTER day/night pair was acquired on 10 July 2011 separated by only 12 h and 4 min. The TIR data (day and night) and the VNIR data (day) were corrected to calibrated VNIR reflectance and TIR temperature and then combined to create an apparent thermal inertia (ATI) image (Fig. 7). Although complexities can arise from changes in atmospheric conditions in the interval between the two scenes, the presence of vegetation on the surface, and shadowing, these are not significant factors for this flow at the time of year of the data collection and the semi-arid conditions. The ATI results show a direct relationship to particle/block size, with fine grained material having a lower ATI than the unmantled blocks (Price et al., 2016). The colorized ATI image draped over a Google Earth image clearly shows this variability and identifies the heavily and moderately mantled regions (Fig. 7). The success of the terrestrial work validated the ATI approach and the methodology is now being applied to decouple the eolian mantling from the underlying lava flows at the Arsia Mons flow field (Ramsey et al., 2012b; Simurda et al., 2015; Crown and Ramsey, 2016).

3.3. Discharge rate

On Earth we commonly work with high temperature thermal emission detected during active effusive events (e.g., Rothery et al., 1988; Oppenheimer, 1991; Wright et al., 2005; Lombardo et al., 2009). Classically, a steady-state thermal model is applied to the data to obtain the time-average discharge rate (TADR) from the energy emission as recorded by the thermal infrared sensor (Harris et al., 2007; Harris and Baloga, 2009; Harris, 2013). This conversion is an empirical solution whereby lava flow area is assumed to increase linearly with TADR (Wright et al., 2001). To solve for TADR, the area of active lava is extracted from the TIR data by applying a single-band, two-component pixel deconvolution model to obtain the fraction of the pixel occupied by high temperature, active lava; and then multiplying by the pixel area to obtain the area of the high temperature source (Harris et al., 1997a, 1997b). For Mars, we have to work with inactive, cold flows, but the same models can be applied to obtain the TADR if the reasoning is inverted. That is, we use the lava flow dimensions obtained from mapping, assume thermal emplacement conditions similar to high-effusion rate channel-fed eruptions on Earth, and estimate the TADR necessary to achieve a given flow area or length.

We explore three methods here that can, or have, been applied to Martian cases. The first was proposed by Crisp and Baloga (1990) and uses a radiative heat loss model to "constrain eruption rates of single-lobed planetary lava flows by assuming thermal characteristics similar to terrestrial flows." The model links TADR to lava flow area (A) through:

$$\mathbf{TADR} = 3f\varepsilon\sigma T_o{}^3 A/\rho c_p(1-\delta_o/h)\cdot\left[\left(T_o{}^3/T_f{}^3\right)-1\right] \tag{7}$$

All parameters used in, and the terrestrially-based assumptions used to solve, this equation are given in Table 4. The second method follows the thermal approach initially applied to TIR data for active flows on Earth and also uses radiative heat that is calculated, again using the lava flow area, from (Pieri and Baloga, 1986),

$$Q_{rad} = \sigma\varepsilon A\left(T_c{}^4 - T_a{}^4\right) \tag{8}$$

so that TADR is obtained through the balance,

$$\mathbf{TADR} = Q_{rad}/\left[\rho\left(c_p\Delta T + \Delta\Phi L_x\right)\right] \tag{9}$$

Finally, the third method uses the relation of Kilburn (2000) to relate the maximum possible flow length to TADR by,

$$l = (3eS/\rho gK)^{1/2}\ \mathbf{TADR}^{1/2} \tag{10}$$

(see Table 4 for all parameters and values). Because area or flow length is the only variable in these three methods, they reduce to linear relations that assume proportionality between TADR and lava flow area or length (Wright et al., 2001). For terrestrial applications, if the relation is set and applied appropriately (i.e., the flow is steady state, has reached its cooling-limited extent, and the model is applied to specific thermal, rheological and topographic conditions, e.g., Harris and Baloga, 2009), then valid TADRs can be retrieved. For the three cases here, the methods reduce to:

$$\textbf{Relation 1: TADR} = 4.32\times10^{-6}\ A \tag{11}$$

$$\textbf{Relation 2: TADR} = 2.08\times10^{-6}\ A \tag{12}$$

$$\textbf{Relation 3: TADR} = \left(l/3.49\times10^{3}\right)^2 \tag{13}$$

Results of applying these three relations to the Arsia Mons units shown in Fig. 6 are given in Table 5. They show reasonable consistency, indicating TADR feeding units in this flow field were of the order of 0.9–7.8 × 10^3 m^3/s. These results are lower, but in a similar range to the values of 3.4–13.0 × 10^3 m^3/s obtained by Wilson and Mouginis-Mark (2001) for a large flank eruption on Elysium Mons. Furthermore, Crisp and Baloga (1990) calculated a model eruption rate of 360 m^3/s for a flow on Ascraeus Mons with a plausible range of 0.01–10.0 × 10^3 m^3/s, depending on the starting assumptions. The results from this study and prior investigations of lava flows found on Tharsis

volcanoes attest to the fact that typical mean output rates on Mars are two to three orders of magnitude higher than those associated with effusive activity on Earth.

3.4. Modelling flow dynamics

We now have the key source term for lava flow modeling, this being TADR (Harris et al., 2015a). We can thus run a lava flow emplacement model to fit to the flow case and to simulate the dynamic, thermal and rheological properties of the flow (e.g., Harris and Rowland, 2001). To do this we take the current version of FLOWGO (Harris and Rowland, 2015) and update it for Martian atmospheric and gravity conditions following Rowland et al. (2004). We then initialize it with the textural and thermal properties of a recent terrestrial basaltic channel-fed lava flow, for example the 2010 Piton de la Fournaise's flow (Rhéty, 2014; Harris et al., 2015b), and use the temperature-dependent viscosity model of Villeneuve et al. (2008). The center line slope profile of the Arsia Mons flow ii (Fig. 6) was input and the model iterated on the measured channel dimension of 175 m by 6 m (with a square channel assumption) until the starting effusion rate was equal to the typical value obtained for this flow (3450 m^3/s). One source of potential error here is assuming the measured channel width approximates the starting channel width. Furthermore, because we cannot be certain of the starting point of this flow it is likely that the starting channel width is smaller than what was used for the model. With those caveats in mind, using the measured channel dimensions, we now iterate on thermal insulation and starting crystallinity until the final flow length of 124 km is matched by the model. This occurs with a modeled lava that has an erupted crystallinity of zero (like those of Kilauea) and quickly develops a nearly-100% insulating crust following the relation (Harris and Rowland, 2001):

$$f_{\mathbf{crust}} = \mathbf{EXP}(-\mathbf{0.00756\ v}) \tag{14}$$

where, f_{crust} is the fraction of the flow surface covered by crust at temperature T_{crust} and v being the flow velocity. We obtain a fit with T_{crust} of 368 K (95 °C). This seems consistent with a flow whose crust has had a long time to cool, which would happen in a slow moving channel extending 10s of kilometers (e.g., Oppenheimer, 1991).

Now we can plot the simulated down channel variation in core temperature, crystallinity, viscosity and velocity (Fig. 8). We find that cooling rates increase from approximately 0 to 1.0 degree K per km at the flow front, with the flow stopping at a temperature of 1352 K (1079 °C), compared with an eruption temperature of 1387 K (1114 °C), so that total down flow cooling is only 35 K. This value is less than comparable terrestrial cooling rates found in channels (e.g., Robert et al., 2014) and is likely the result of the extreme insulation

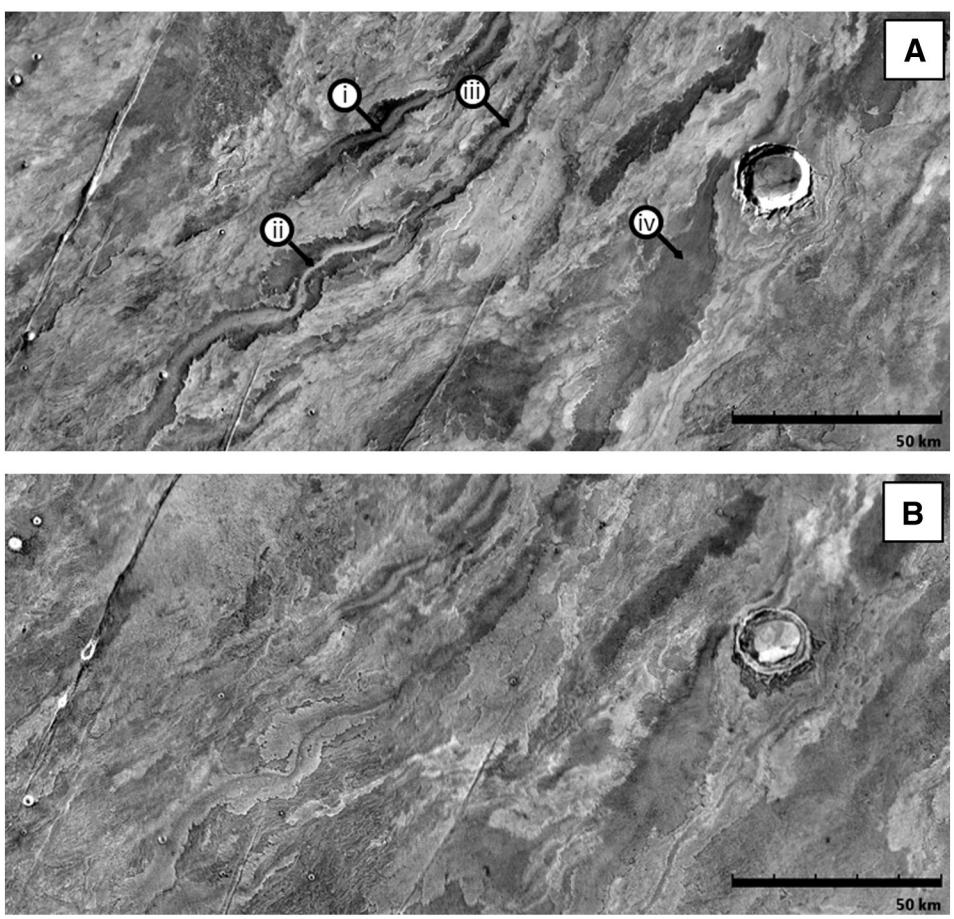

Fig. 6. A portion of the Arsia Mons southwest flow field centered at 238.0E, 23.1S on four channeled lava flows (i, ii, iii, iv) that are modeled in the fourth case study. The thermophysical variability of the different flows (including flows that stay cool and stay warm throughout the diurnal cycle) can also be seen where comparing (A) and (B). (A) THEMIS day IR 100 m (v. 12) global mosaic (Edwards et al., 2011) showing the cooler flow margins and warmer central channel of flows i, ii and iii, which could be mantled by eolian fines or contain lava that is rheologically-different than the levees. (B) THEMIS night IR 100 m (v. 14) global mosaic (Edwards et al., 2011) highlighting less-mantled flows and flow margins by their warmer temperatures (as high as 247 K). **(C)** THEMIS day IR mosaic colorized using THEMIS night IR data with areas of red and orange indicating the warmest (rockiest) portions of the flows. White box denotes the area in (D). **(D)** Mosaic of two Context (CTX) Camera images (Image ID P04_002711_1560_XN_24S122W and P01_001590_1567_XN_23S122W) of flow ii. Yellow and white arrows indicate the modeled channel width and flow width, respectively. (For interpretation of the references to color in this figure legend, the reader is referred to the web version of this article.)

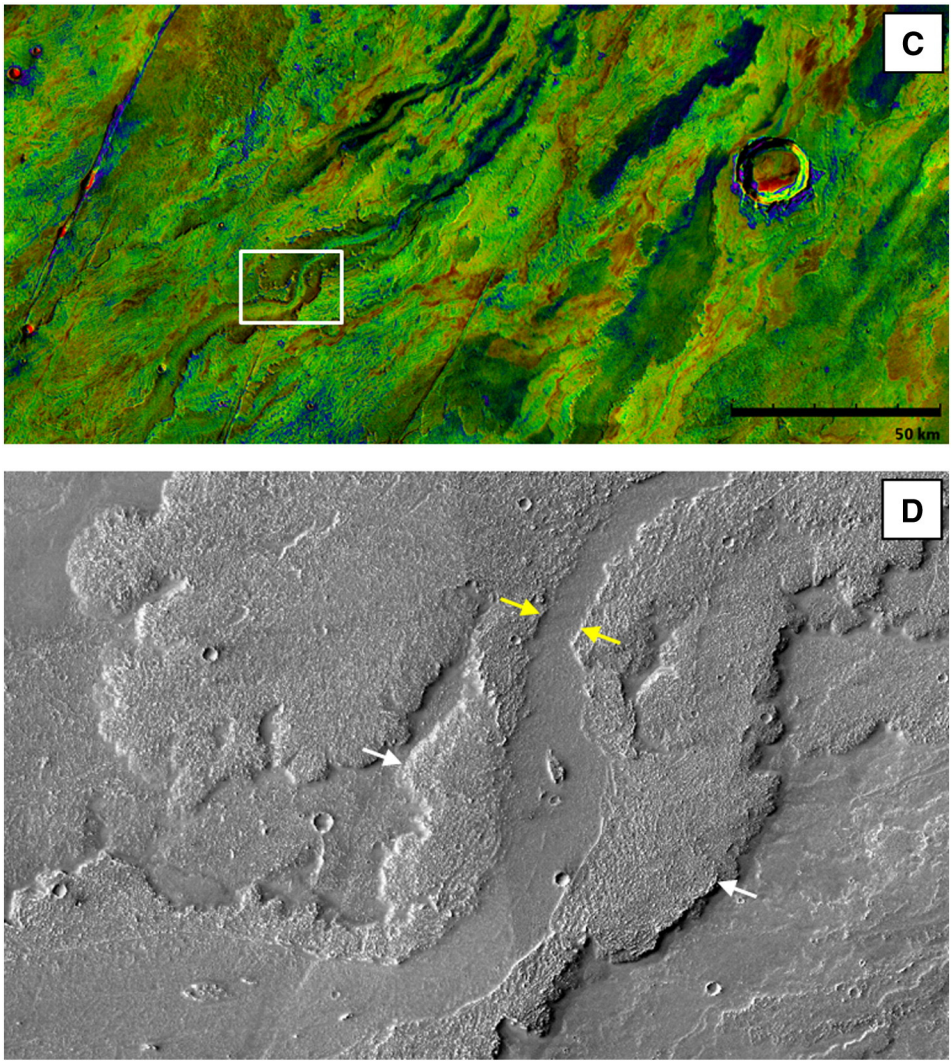

Fig. 6 (*continued*).

(e.g., Keszthelyi et al., 2000). Crystal content increases to 23% at the flow front, causing the mixture viscosity to increase to 10^3 Pa s. Finally, we see that flow velocity declines from around 4–5 m/s at the vent, to between 0.1 and 3 m/s in the medial-to-distal section, not dissimilar to the viscosity profile obtained down Mauna Loa's 1984 channel (Lipman and Banks, 1987). We also see the effect of breaks in slope on the velocity profile, which cause peaks in the general trend. In summary, model-derived flow thermo-rheological properties, and their variation down flow, are nearly identical to those found terrestrially, the main difference being an order of magnitude higher discharge rate, which leads to flow system dimensions that are typically an order of magnitude greater on Mars.

4. Trends

One rather simple analysis approach to understand how TIR data are being applied to volcanic questions is to examine the number of publications using key search terms. The trend over time of these results for both Earth and Mars also reveals how scientific results are related to new missions/instruments and perhaps more interestingly, allow us to project into the future. While it may be generally true that the number of publications follows the cadence of the number of missions, this is not always the case. Scientists will utilize available data to answer a scientific question, even if those data are archival. What is more important is the question, "Are TIR data being used for scientifically important studies of volcanic processes (as opposed to a decline in favor of another technology or in the interest in volcanic processes)?". We chose a simple approach for this analysis using multiple Google Scholar searches, continually refining the search terms. We have made no attempt to separate these results based on the impact factor of the journal or the h-index of the paper itself. The results are simply meant as a guide to the trend of TIR data applied to volcanology for Earth and Mars.

The sheer number and variety of TIR instruments launched into Earth orbit has been far greater than for Mars, and the number of volcanic studies published over time is of little surprise (Table 6). This number is now nearly eight times greater than the number of similar studies on Mars. A Google Scholar search on the strings "Earth-infrared" and "Mars-infrared" returned 2,580,000 and 71,900 results, respectively (search date: 31 May 2015). Once the search terms were narrowed to constrain the data to thermal infrared and the studies to volcanology, the numbers were reduced to 5054 and 643 for the Earth and Mars, respectively (Table 6). The vast array of Earth-based infrared sensors and active-volcanic applications explains the difference, but the quantity of research on Mars in the realm of thermal infrared remote sensing implied by this result remains impressive.

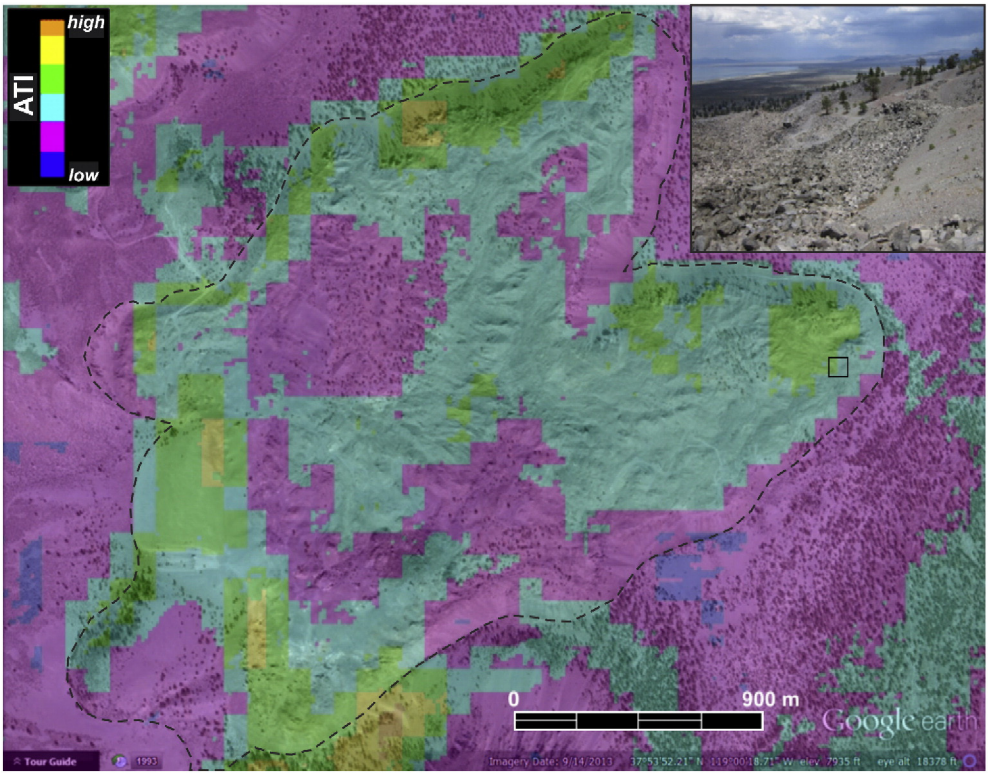

Fig. 7. ASTER-based apparent thermal inertia (ATI) image of the North Coulee rhyolite flow (outlined with the dashed line), Mono Craters, CA draped over a Google Earth image acquired 2 months later. The colorized ATI image has been scaled from low ATI values (blue and magenta) signifying fine-grained pyroclastic airfall mantling deposits to high ATI values (yellow and orange) denoting unmantled blocks larger than 10 cm. The inset photograph corresponds to the small black box and shows the contact between these two surfaces.

Plotting the results over time shows that Mars research using the thermal infrared has increased with approximately the same exponential rate as for the Earth, but delayed by 30 years (Fig. 9). Although both trends follow this exponential growth with time, a distinct inflection point is present for Mars after 2000. No such inflection point is obvious for Earth, which denotes the continuous presence of satellites with TIR instruments since the mid-1960s. If one focuses on all TIR studies rather than just those of volcanic studies, the relationship between new instrumentation and new publications becomes even more obvious. For Mars, three inflection points become visible: (1) in 1965 when the publication rate increased from 6 to 10 per year to 26 per year; (2) in 1990 when the publication rate increased from 16 to 20 per year to 45 per year; and then (3) in 2000 when the publication rate increased from 20 to 58 per year to 160–370 per year. These inflections respectively followed (1) the Mars flyby missions by the early Mariner missions; (2) analysis of older TIR data from the Viking (US) and Phobos (Soviet Union) missions in preparation for the planned TIR data from the Mars Observer and Mars Global Surveyor missions; and (3) the arrival of new the TIR instruments, THEMIS (orbital) and mini TES (rover). If we project the Mars-based trend to 2050 (Fig. 9), the result is similar to that of Earth. However, the lack of planned future missions to Mars with TIR capabilities means that this accelerating publication record will likely fall-off,

Table 4
Values used to solve Eqs. (7), (8), (9) and (10) and generate relations 1, 2 and 3.

Parameter	Symbol	Value	Units	Source
Hot fraction	f	0.0081		Kilauea channel: Flynn and Mouginis-Mark (1994)
Emissivity	ε	0.95		Basaltic 'a'a (Kilauea): Harris (2013)
Stefan-Boltzman constant	σ	5.67E−08	W/m K^4	
Eruption temperature	T_o	1413	K	Mauna Loa 1984: Lipman and Banks (1987)
Bulk density	ρ	1850	kg/m^3	Mauna Loa 1984: Lipman and Banks (1987)
Specific heat	c_p	1150	J/kg K	Kilburn (2000)
Crust thickness	δ_o	0.85	m	Mauna Ulu 1974: Harris et al. (2009)
Flow thickness	h	3	m	Mauna Ulu 1974: Harris et al. (2009)
Stop temperature	T_f	980	°C	Mauna Loa 1984: Harris and Rowland (2015)
Crust temperature	T_c	423	K	Lonquimay 1991: Oppenheimer (1991)
Ambient temperature	T_a	−54	219	see Table 1
Latent heat	L_x	3.50E+05	J/kg	
Fractional cystallization	Δ_Φ	0.45		Mauna Loa 1984: Harris and Rowland (2015)
Cooling range	ΔT	225		$= T_o - T_f$
Energy for flow front failure	eS	2.00E+04	J/m	Kilburn (2000)
Gravity	g	3.8	m/s^2	see Table 1
Thermal diffusivity of basalt	K	7.00E−07	m^2/s	Turcotte and Schubert (2002)

Table 5
Flow measurements used to solve the three TADR relations of Eqs. (11), (12) and (13), with the results from applying the relations to flow units i, ii, iii and iv of Fig. 6.

Arsia Mons Flow	Length (km)	Area (m2)	Q_{rad} (W)	TADR Relation 1 (m^3/s)	TADR Relation 2 (m^3/s)	TADR Relation 3 (m^3/s)
i	103,710	5.98E+08	9.57E+11	2584	1243	882
ii	123,514	9.19E+08	1.47E+12	3971	1909	1251
iii	111,553	6.76E+08	1.08E+12	2920	1404	1021
iv	163,102	1.80E+09	2.89E+12	7796	3749	2182

Table 6
Google Scholar search (31 May 2015) using the Boolean string for Mars: ["*thermal infrared*" + (*volcano OR volcanic OR lava*) + *Mars -lunar -moon -Io -Jupiter*]; Earth: ["*thermal infrared*" + (*volcano OR volcanic OR lava*) *-lunar -moon -Mars -Io -Jupiter*]; Moon: ["*thermal infrared*" + (*volcano OR volcanic OR lava*) + *lunar* + *moon -Io -Jupiter -Mars*]; and Io: ["*thermal infrared*" + (*volcano OR volcanic OR lava*) + *Io* + *Jupiter -lunar -moon -Mars*]. The search terms were chosen to minimize the influence of false positive results for studies: (1) focused on other planets; (2) using other infrared wavelength regions; and/or (3) infrared studies of other geologic processes. Results are given for five year periods from 1950 to 2014 and for the year 2015.

Body	Total	1950–2014	2015
Earth	5054	4905	149
Mars	643	624	19
Moon	146	142	4
Io	22	20	2

which may already be occurring. The average number of volcanic publications per year for Mars using TIR data was 34.2 between 2005 and 2009, which then increased to 57.6 during 2010–2014. However, for the first part of 2015 this rate was only 3.8. We expect that this will likely not be the case for terrestrial studies due to new and planned TIR instruments slated for land, sea and atmospheric studies. For example, the Thermal Infrared Sensor (TIRS) instrument on Landsat 8, the planned Ecosystem Spaceborne Thermal Radiometer Experiment on Space Station (ECOSTRESS) instrument to be placed on the International Space Station, and the notional Hyperspectral Infrared Imager (HyspIRI) orbital instrument should continue to provide higher spatial resolution TIR data for the Earth.

The exponential growth of study in the field of TIR remote sensing of both planets is certainly a reflection of the instrumentation and data available, as well as the ever-increasing ease in acquiring and processing these data (Harris, 2013). However, the preponderance of Earth-based studies is also, of course, a function of the greater diversity of volcanic processes on Earth coupled with the direct risk presented by volcanic activity to human populations. Thermal IR data from Earth orbit have been acquired continuously for over a half century from the earliest weather satellites (e.g., TIROS, VHRR, AVHRR), through the Landsat series of missions and continuing with instruments such as ASTER, Earth Observing-1 (EO-1), Moderate Resolution Imaging Spectroradiometer (MODIS) and Spinning Enhanced Visible and Infrared Imager (SEVIRI) that operate along with the older workhorse weather satellites. Although these data have been acquired at various spatial, spectral and temporal scales, none of these instruments were designed solely for the study of volcanic processes (Harris, 2013).

Conversely, Mars TIR instrument technologies, and the resulting data, have outpaced those of Earth in terms of volcanological applications. There have been far fewer missions to Mars, but nearly all have contained some form of thermal infrared instrument until the latest set of missions. Planetary instruments are generally seen as experimental in nature and therefore technologies, such as hyperspectral resolution and new detector design, commonly appear first for Mars

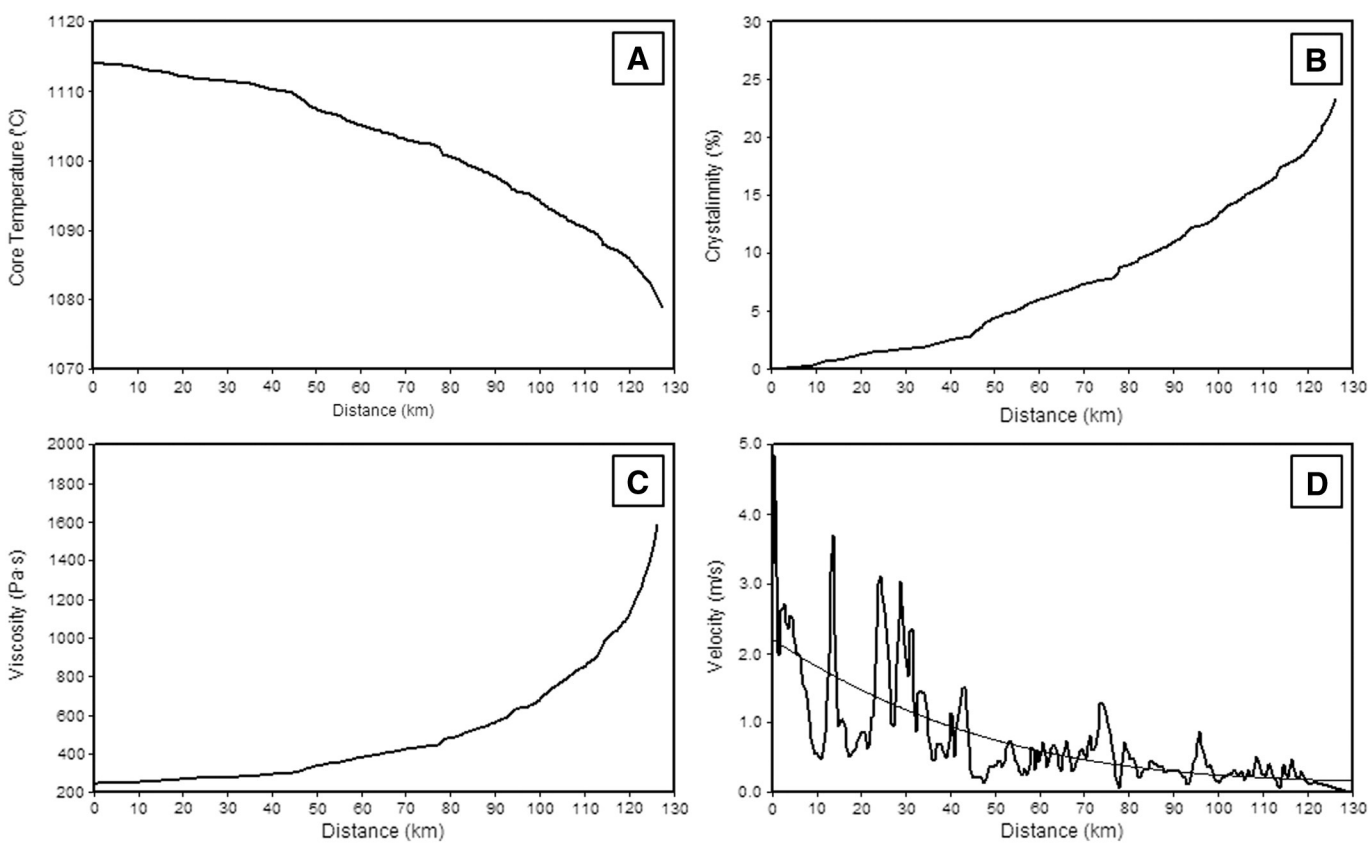

Fig. 8. Output of the FLOWGO model modified for Mars conditions and applied to the Arsia Mons flow shown in Fig. 6. (A) Core temperature versus flow distance. (B) Crystallinity versus flow distance. (C) Viscosity versus flow distance. (D) Velocity versus flow distance. A third-order polynomial fit to the velocity is also shown with the thin line.

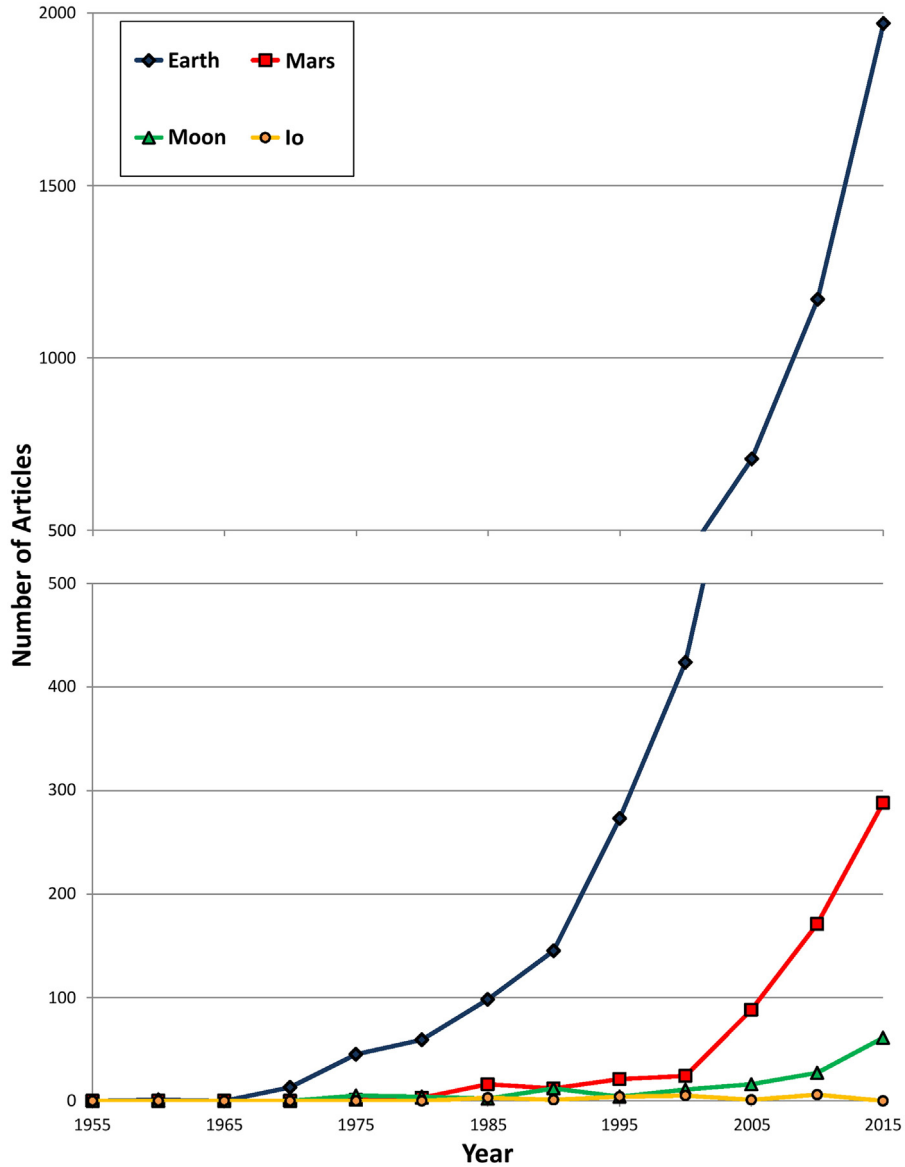

Fig. 9. Plot of all articles found using Google Scholar that contain the terms "thermal infrared" and "volcano" or "volcanic" or "lava" and the planet name (see Table 6). Although all follow an exponential growth with time, distinct inflection points are present for Mars and the moon due to the arrival of new TIR instruments in orbit. For example, the arrival of the Diviner instrument on Lunar Reconnaissance Orbiter (LRO) resulted in an increase in the number of publications over the past five years.

missions, later perhaps being adapted for Earth. Earth-orbiting instruments, on the other hand, are typically treated as a part of longer-term record keeping and therefore technology improvements are much slower to come online, in favor of baseline data continuity.

5. Conclusions

The specific focus of this paper, as well as our original talk at the Geological Society of America Meeting in 2014, centers on how thermal infrared remote sensing is being used to understand volcanic processes, both past and present on Earth and Mars. New and innovative studies arising on one planet using a specific dataset, or combination of datasets, can be used as a blueprint for analysis of the other. In this regard, inter-connected regimes of advances in instrument technology, data analysis/modeling and their integration can feed back between Earth and Mars to allow better understanding of geologic processes that operate on both planets.

Because the volcanological questions and problems arising on Earth are quite different from those on Mars, the focus of TIR studies for both these planets is also quite different. Studies from Earth orbit have focused primarily on temperature analyses and active processes; whereas those from Mars orbit have centered on the spectral and thermophysical. Clearly, the lack of active volcanic processes, colder surface temperatures and the commonly dusty conditions on Mars has driven the design of TIR instrumentation, with a focus on spectral and spatial improvements, over temporal.

Despite the differences in volcanic processes and orbital TIR instrumentation for both planets, a convergence of the analysis and modeling techniques has begun as the datasets and algorithms continue to improve. There exists a rather large and untapped potential in using these data for quantitative comparative studies of volcanic processes with the benefit of being able to validate the results on Earth. We have highlighted several of these cross-over approaches, which are equally applicable for examining volcanic surfaces on both planets. For example, spectral deconvolution and thermal inertia analysis have been the dominant approaches for Mars data analysis, and are now being adapted for volcanic studies on Earth. Similarly, analysis and modeling techniques designed for high-temporal resolution data of surface temperature and radiant flux on Earth can be adapted for the older flows on Mars. A common thread in all of these studies is the critical

need for high-resolution data to validate the modeling approaches and allow for a hierarchical approach to scaling over orders of magnitude resolution differences. This can be found in studies of terrestrial volcanism using hand-held thermal IR cameras as well as TIR data returned from the surface of Mars from the mini-TES instrument that have improved the accuracy of the orbital data (e.g., Christensen et al., 2001; Harris et al., 2007; Ramsey et al., 2012a; Ruff et al., 2014). Furthermore, as spatial resolution from orbit improves, sub-1 m data (e.g., HiRISE at Mars, WorldView at Earth, etc.) provide the contextual scale common to most ground-based studies thereby expanding the analyses to include new end-members and categories.

Acknowledgments

Funding for MSR during the lifetime of the ASTER project was made possible through the NASA Science of Terra and Aqua Program (grant numbers: NNG04GO69G, NNX08AJ91G, NNX11AL29G, NNX14AQ96G). Additional funding for MSR and DAC was provided by the NASA Planetary Geology and Geophysics Program (grant number: NNX11AP17G). MSR would like to thank the many ASTER-URP investigators, collaborators and students who devoted their time and skills to the project over the years, including: S. Belousov, M. Belousova, A. Carter, J. Dehn, K. Duda, O. Girina, H. Morgan, M. Patrick, E. Pilger, S. Rose, A. Steffke, M. Watson, P. Webley, R. Wessels, and R. Wright. The authors would also like to thank J. Bandfield and V. Hamilton, whose detailed reviews greatly improved the quality of this manuscript.

References

Bandfield, J.L., 2009. Effects of surface roughness and graybody emissivity on martian thermal infrared spectra. Icarus 202, 414–428.

Bandfield, J.L., Hamilton, V.E., Christensen, P.R., 2000. A global view of Martian surface compositions from MGS-TES. Science 287, 1626–1630.

Bandfield, J.L., Hamilton, V.E., Christensen, P.R., McSween Jr., H.Y., 2004. Identification of quartzofeldspathic materials on Mars. J. Geophys. Res. 109, E10009. http://dx.doi.org/10.1029/2004JE002290.

Bandfield, J.L., Edwards, C.S., Montgomery, D.R., Brand, B.D., 2013. The dual nature of the martian crust: young lavas and old clastic materials. Icarus 222 (1), 188–199.

Bleacher, J.E., Williams, D.A., Mouginis-Mark, P.J., Shean, D., Greeley, R., 2013. Geologic map of the Olympus Mons volcano, Mars. Lunar and Planetary Science Conference #XLIV, abstract #2074.

Bulletin Global Volcanism Network (BGVN), 2005. Shiveluch Volcano. 30. Smithsonian Institution, Washington, D.C., p. 02.

Buongiorno, M.F., Realmuto, V.J., Doumaz, F., 2002. Recovery of spectral emissivity from thermal infrared multispectral scanner imagery acquired over a mountainous terrain: a case study from Mount Etna Sicily. Remote Sens. Environ. 79, 123–133.

Bursik, M., Sieh, K., 1989. Range front faulting and volcanism in the Mono Basin, Eastern California. J. Geophys. Res. 94, 15587–15609.

Byrnes, J.M., Ramsey, M.S., Crown, D.A., 2004. Surface unit characterization of the Mauna Ulu flow field, Kilauea volcano, Hawai'i using integrated field and remote sensing analyses. J. Volcanol. Geotherm. Res. 135, 169–193.

Cai, G., Xue, Y., Hu, Y., Wang, Y., Guo, J., Luo, Y., Wu, C., Zhong, S., Qi, S., 2007. Soil moisture retrieval from MODIS data in Northern China Plain using thermal inertia model. Int. J. Remote Sens. 28 (16), 3567–3581.

Carr, M.H., 1973. Volcanism on Mars. J. Geophys. Res. 78, 4049–4062.

Carr, M.H., Baum, W.A., Blasius, K.R., Briggs, G.A., Cutts, J.A., Duxbury, T.C., Greeley, R., Guest, J., Masursky, H., Smith, B.A., 1980. Viking Orbiter Views of Mars. NASA Special Publication 441. U.S. Government Printing Office, Washington, DC (136 pp).

Carter, A.J., Ramsey, M.S., Durant, A.J., Skilling, I.P., Wolfe, A.L., 2009. Micron-scale roughness of volcanic surfaces from thermal infrared spectroscopy and scanning electron microscopy. J. Geophys. Res. 114. http://dx.doi.org/10.1029/2008JB005632.

Cattermole, P., 1996. Planetary Volcanism: A Study of Volcanic Activity in the Solar System. second ed. Praxis Publishing, Chichester, UK (417 p).

Chicarro, A.L., Scoon, G.E.N., Coradini, M., 1989. Mission to Mars, Report of the Mars Exploration Study Team. European Space Agency, Paris (ESA SP-1117, 138 p., ISBN 92–9092-040-8).

Christensen, P.R., 1986. Regional dust deposits on Mars: physical properties, age, and history. J. Geophys. Res. 91 (B3), 3533–3545.

Christensen, P.R., Morris, R.V., Lane, M.D., Bandfield, J.L., Malin, M.C., 2001. Global mapping of Martian hematite mineral deposits: remnants of water-driven processes on early Mars. J. Geophys. Res. 106, 23873–23885.

Christensen, P.R., Wyatt, M.B., Glotch, T.D., Rogers, A.D., Anwar, S., Arvidson, R.E., Bandfield, J.L., Blaney, D.L., Budney, C., Calvin, W.M., Fallacaro, A., Fergason, R.L., Gorelick, N., Graff, T.G., Hamilton, V.E., Hayes, A.G., Johnson, J.R., Knudson, A.T., McSween Jr., H.Y., Mehall, G.L., Mehall, L.K., Moersch, J.E., Morris, R.V., Smith, M.D., Squyres, S.W., Ruff, S.W., Wolff, M.J., 2004. Mineralogy at meridiani planum from the mini-TES experiment on the Opportunity Rover. Science 306, 1733–1739.

Christensen, P.R., McSween, H.Y., Bandfield, J.L., Ruff, S.W., Rogers, A.D., Hamilton, V.E., Moersch, J.E., 2005. Evidence for magmatic evolution and diversity on Mars from infrared observations. Nature 436, 504–509.

Conrath, B.J., 1975. Thermal structure of the Martian atmosphere during the dissipation of the dust storm of 1971. Icarus 24, 36–46.

Crisp, J., Baloga, S., 1990. A model for lava flows with two thermal components. J. Geophys. Res. 95, 1255–1270.

Crisp, J., Kahle, A.B., Abbott, E.A., 1990. Thermal infrared spectral character of Hawaiian basaltic glasses. J. Geophys. Res. 95, 21657–21669.

Crown, D.A., 2015. Geologic map of MTM-25127 and -25122 Quadrangles. Daedalia Planum Region of Mars. United States Geological Survey Map (in preparation).

Crown, D.A., Greeley, R., 1993. Volcanic geology of hadriaca patera and the eastern Hellas region of Mars. J. Geophys. Res. 98, 3431–3451.

Crown, D.A., Greeley, R., 2007. Geologic Map of MTM-30262 and -30267 Quadrangles, Hadriaca Patera Region of Mars. United States Geological Survey Scientific Investigations Series Map 2936, scale 1:1,004,000.

Crown, D.A., Ramsey, M.S., 2016. Morphologic and thermophysical characteristics of lava flows southwest of Arsia Mons, Mars. J. Volcanol. Geotherm. Res. (in review).

Crown, D.A., Berman, D.C., Ramsey, M.S., 2015. Lava Flow Fields of Southern Tharsis, Mars: Flow Types, Interactions, and Ages, Lunar Planetary Science Conference #XLVI, Abstract #1439.

Dean, K.G., Servilla, M., Roach, A., Foster, B., Engle, K., 1998. Satellite monitoring of remote volcanoes improves study efforts in Alaska. EOS Trans. Am. Geophys. Union 79 (413), 422–423.

Del Negro, C., Fortuna, L., Herault, A., Vicari, A., 2008. Simulations of the 2004 lava flow at Etna volcano using the magflow cellular automata model. Bull. Volcanol. 70, 805–812. http://dx.doi.org/10.1007/s00445-007-0168-8.

Edwards, C.S., Christensen, P.R., Hamilton, V.E., 2008. Evidence for extensive olivine-rich basalt bedrock outcrops in Ganges and Eos chasmas, Mars. J. Geophys. Res. 113. http://dx.doi.org/10.1029/2008JE003091.

Edwards, C.S., Nowicki, K.J., Christensen, P.R., Hill, J., Gorelick, N., Murray, K., 2011. Mosaicking of global planetary image datasets: 1. Techniques and data processing for Thermal Emission Imaging System (THEMIS) multi-spectral data. J. Geophys. Res. Planets 116. http://dx.doi.org/10.1029/2011JE003857.

Fagents, S.A., Lanagan, P., Greeley, R., 2002. Rootless cones on Mars: a consequence of lava-ground ice interaction. In: Smellie, J.L., Chapman, M.G. (Eds.), Volcano–Ice Interaction on Earth and Mars. Geological Society Special Publication 202, pp. 295–318.

Favalli, M., Pareschi, M.T., Neri, A., Isola, I., 2005. Forecasting lava flow paths by a stochastic approach. Geophys. Res. Lett. 32. http://dx.doi.org/10.1029/2004GL021718.

Fergason, R.L., Christensen, P.R., Kieffer, H.H., 2006. High-resolution thermal inertia derived from the Thermal Emission Imaging System (THEMIS): thermal model and applications. J. Geophys. Res. 111. http://dx.doi.org/10.1029/2006JE002735.

Flynn, L.P., Mouginis-Mark, P.J., 1994. Temperature of an active lava channel from spectral measurements, Kilauea volcano, Hawaii. Bull. Volcanol. 56, 297–301.

Francis, P.W., Wood, C.A., 1982. Absence of silicic volcanism on Mars: implications for crustal composition and volatile abundance. J. Geophys. Res. 88, 8333–8344.

Frankel, C., 1996. Volcanoes of the Solar System. Cambridge University Press, Cambridge, UK (232 pp).

Ganci, G., Vicari, A., Bonfiglio, S., Gallo, G., Del Negro, C., 2011. A texton-based cloud detection algorithm for MSG-SEVIRI multispectral images. Geomatics, Nat. Hazards Risk 2, 279–290.

Garry, W.B., Williams, D.A., Bleacher, J.E., 2014. Geologic mapping of Arsia and Pavonis Montes, Mars. Lunar and Planetary Science Conference #XLV abstract #2133.

Gillespie, A.R., 1992. Enhancement of multispectral thermal infrared images: decorrelation contrast stretching. Remote Sens. Environ. 42, 147–155.

Gouhier, M., Harris, A., Calvari, S., Labazuy, P., Guéhenneux, Y., Donnadieu, F., Valade, S., 2011. Lava discharge during Etna's January 2011 fire fountain tracked using MSG-SEVIRI. Bull. Volcanol. 1–7 http://dx.doi.org/10.1007/s00445–011-0572-y.

Greeley, R., 2007. Planetary Landscapes. Chapman & Hall, New York, NY (286 p).

Greeley, R., Crown, D.A., 1990. Volcanic geology of tyrrhena patera, Mars. J. Geophys. Res. 95, 7133–7149.

Greeley, R., Spudis, P.D., 1981. Volcanism on Mars. Rev. Geophys. 19, 13–41.

Greeley, R., Fagents, S.A., Bridges, N.T., Crown, D.A., Crumpler, L.S., Mouginis-Mark, P.J., Zimbelman, J.R., 2000. Volcanism on the Red Planet: Mars. In: Zimbelman, J.R., Gregg, T.K.P. (Eds.), Environmental Effects on Volcanic Eruptions: from Deep Oceans to Deep Space. Kluwer Academic/Plenum Publishers, New York (266 pp).

Gregg, T.K.P., Crown, D.A., Farley, M.A., 2015. Geologic Map of MTM −15257 and −20257 Quadrangles, Tyrrhenus Mons, Mars. United States Geological Survey Map (in review).

Hamilton, V.E., Christensen, P.R., McSween, H.Y., Bandfield, J.L., 2003. Searching for the source regions of Martian meteorites using MGS TES: integrating Martian meteorites into the global distribution of igneous materials on Mars. Meteorit. Planet. Sci. 38, 871–885.

Hamilton, C.W., Fagents, S.A., Thordarson, T., 2010. Explosive lava-water interactions II: self-organization processes among volcanic rootless eruption sites in the 1783–1784 Laki lava flow, Iceland. Bull. Volcanol. 72, 469–485. http://dx.doi.org/10.1007/s00445-009-0331-5.

Hapke, B., 2012. Theory of Reflectance and Emittance Spectroscopy. second ed. Cambridge University Press, New York, NY (529 pp. ISBN: 978–0-521-88349-8).

Harris, A.J.L., 2013. Thermal Remote Sensing of Active Volcanoes: A User's Manual. Cambridge University Press, New York, NY (ISBN: 978–0-521-885945-5. 736 pp).

Harris, A.J.L., Baloga, S.M., 2009. Lava discharge rates from satellite-measured heat flux. Geophys. Res. Lett. 36, L19302. http://dx.doi.org/10.1029/2009GL039717.

Harris, A.J.L., Rowland, S.K., 2001. FLOWGO: a kinematic thermorheological model for lava flowing in a channel. Bull. Volcanol. 63, 20–44. http://dx.doi.org/10.1007/s004450000120.

Harris, A.J.L., Rowland, S.K., 2015. FLOWGO 2012: an updated framework for thermorheological simulations of channel-contained lava. In: Carey, R., Cayol, V., Poland, M., Weis, D. (Eds.), Hawaiian Volcanoes: From Source to Surface, AGU Special Monograph 208, Hawaiian Volcanoes: From Source to Surface, pp. 457–482.

Harris, A.J.L., Blake, S., Rothery, D.A., Stevens, N.F., 1997a. A chronology of the 1991 to 1993 Etna eruption using AVHRR data: implications for real time thermal volcano monitoring. J. Geophys. Res. 102, 7985–8003.

Harris, A.J.L., Butterworth, A.L., Carlton, R.W., Downey, I., Miller, P., Navarro, P., Rothery, D.A., 1997b. Low cost volcano surveillance from space: case studies from Etna, Krafla, Cerro Negro, Fogo, Lascar and Erebus. Bull. Volcanol. 59, 49–64.

Harris, A.J.L., Pilger, E., Flynn, L.P., 2002. Web-based hot spot monitoring using GOES: what it is and how it works. Adv. Environ. Monit. Model. 1 (3), 5–36.

Harris, A., Pirie, D., Horton, K., Garbeil, H., Pilger, E., Ramm, H., Hoblitt, R., Thornber, C., Ripepe, M., Marchetti, E., Poggi, P., 2005. DUCKS: low cost thermal monitoring units for near-vent deployment. J. Volcanol. Geotherm. Res. 143, 335–360.

Harris, A.J., Dehn, J., Calvari, S., 2007. Lava effusion rate definition and measurement: a review. Bull. Volcanol. 70, 1–22. http://dx.doi.org/10.1007/s00445-007-0120-y.

Harris, A.J., Favalli, M., Mazzarini, F., Hamilton, C.W., 2009. Construction dynamics of a lava channel. Bull. Volcanol. 71, 459–474. http://dx.doi.org/10.1007/s00445-008-0238-6.

Harris, A.J., Rhéty, M., Gurioli, L., Villeneuve, N., Paris, R., 2015a. Simulating the thermorheological evolution of channel-contained lava: FLOWGO and its implementation in EXCEL. In: Harris, A.J.L., De Groeve, T., Garel, F., Carn, S.A. (Eds.), Detecting, Modelling and Responding to Effusive Eruptions. Geological Society London, Special Publications 426.

Harris, et al., 2015b. Conclusion: recommendations and findings of the RED SEED working group. In: Harris, A.J.L., De Groeve, T., Garel, F., Carn, S.A. (Eds.), Detecting, Modelling and Responding to Effusive Eruptions. Geological Society London, Special Publications 426.

Hildreth, W., 2004. Volcanological perspectives on Long Valley, Mammoth Mountain, and mono craters: several contiguous but discrete systems. J. Volcanol. Geotherm. Res. 136, 169–198.

Hodges, C.A., Moore, H.J., 1994. Atlas of volcanic landforms on Mars. United States Geological Survey Professional Paper 1534 (194 pp).

Hunt, G.R., 1980. Electromagnetic radiation: the communication link in remote sensing. In: Siegel, B.S., Gillespie, A.R. (Eds.), Remote Sensing in Geology. John Wiley, New York, NY, pp. 5–45.

Johnson, J.R., Christensen, P.R., Lucey, P.G., 2002. Dust coatings on basaltic rocks and implications for thermal infrared spectroscopy of Mars. J. Geophys. Res. 107 http://dx.doi.org/10.1029/2000JE001405.

Kahle, A.B., 1987. Surface emittance, temperature, and thermal inertia derived from thermal infrared multispectral scanner (TIMS) data for Death Valley, California. Geophysics 52, 858–874.

Kahle, A.B., Gillespie, A.R., Abbott, E.A., Abrams, M.J., Walker, R.E., Hoover, G., Lockwood, J.P., 1988. Relative dating of Hawaiian lava flows using multispectral thermal infrared images: a new tool for geologic mapping of young volcanic terranes. J. Geophys. Res. 93, 15239–15251.

Keszthelyi, L., McEwen, A.S., Thordarson, T., 2000. Terrestrial analogs and thermal models for Martian flood lavas. J. Geophys. Res. 105, 15027–15049.

Kieffer, H.H., Martin, T.Z., Peterfreund, A.R., Jakosky, B.M., Miner, E.D., Palluconi, F.D., 1977. Thermal and albedo mapping of Mars during the Viking primary mission. J. Geophys. Res. 82, 4249–4291.

Kilburn, C.R.J., 2000. Lava flows and flow fields. In: Sigurdsson, H., Houghton, B., McNutt, S., Rymer, H., Stix, J. (Eds.), Encyclopedia of Volcanoes. Academic Press, San Diego, pp. 291–305.

King, P.L., Lee, R.J., Ramsey, M.S., McCutcheon, W.A., Dufresne, C.D.M., Shearer, C.K., 2011. Using thermal infrared spectroscopy of glasses to unravel composition and thermal history—a new thermometer for lunar glass beads? Lunar Planetary Science Conference #XLII abstract #2069

Koeppen, W.C., Hamilton, V.E., 2008. Global distribution, composition, and abundance of olivine on the surface of Mars from thermal infrared data. Journal of Geophysical Research 113, E05001. http://dx.doi.org/10.1029/2007JE002984.

Kraft, M.D., Michalski, J.R., Sharp, T.G., 2003. Effects of pure silica coatings on thermal emission spectra of basaltic rocks: considerations for Martian surface mineralogy. Geophys. Res. Lett. 30. http://dx.doi.org/10.1029/2003GL018848.

Krippner, J.B., Ramsey, M.S., 2013. Pyroclastic flow and lahar hazards in populous, developing regions: Integrated TIR and SAR data analysis. IAVCEI General Assembly Program, abstract #4W_2E-P19, p. 458.

Lang, N.P., Tornabene, L.L., McSween, H.Y., Christensen, P.R., 2009. Tharsis-sourced relatively dust-free lavas and their possible relationship to Martian meteorites. J. Geophys. Res. 185, 103–115.

Lipman, P., Banks, N.G., 1987. AA flow dynamics, Mauna Loa 1984. U. S. Geol. Surv. Prof. Pap. 1350, 1527–1567.

Lombardo, V., Harris, A.J.L., Calvari, S., Buongiorno, M.F., 2009. Spatial variations in lava flow field thermal structure and effusion rate derived from very high spatial resolution hyperspectral (MIVIS) data. J. Geophys. Res. 114 (B02208). http://dx.doi.org/10.1029/2008JB005648.

Lyon, R.J.P., 1965. Analysis of rocks by spectral infrared emission (8 to 25 microns). Econ. Geol. 60, 715–736.

Mandt, K.E., de Silva, S.L., Zimbelman, J.R., Crown, D.A., 2008. Origin of the medusae fossae formation, Mars: insights from a synoptic approach. J. Geophys. Res. 113, E12011. http://dx.doi.org/10.1029/2008JE003076.

McGetchin, T.R., Repin, R.O., Phillips, R.J., 1981. Basaltic volcanism on the terrestrial planets. Basaltic Volcanism Study Project. Pergamon Press, Inc., New York (1286 pp).

McSween, H.Y., Ruff, S.W., Morris, R.V., Bell, J.F., Herkenhoff, K., Gellert, R., Stockstill, K.R., Tornabene, L.L., Squyres, S.W., Crisp, J.A., Christensen, P.R., 2006. Alkaline volcanic rocks from the Columbia Hills, Gusev crater, Mars. J. Geophys. Res. 111 (E9). http://dx.doi.org/10.1029/2006JE002698.

Michalski, J.R., Kraft, M.D., Sharp, T.G., Williams, L.B., Christensen, P.R., 2005. Mineralogical constraints on the high-silica Martian surface component observed by TES. Icarus 174, 161–177.

Minitti, M.E., Hamilton, V.E., 2010. A search for basaltic-to-intermediate glasses on Mars: assessing martian crustal mineralogy. Icarus 210, 135–149.

Moersch, J.E., Christensen, P.R., 1995. Thermal emission from particulate surfaces: a comparison of scattering models with measured spectra. J. Geophys. Res. 100, 7465–7477.

Mouginis-Mark, P.J., Wilson, L., Zuber, M.T., 1992. The physical volcanology of Mars. In: Kiefer, H.H., Jakosky, B.M., Snyder, C.W., Mathews, M.S. (Eds.), Mars. University of Arizona Press, Tucson, pp. 424–452.

Mouginis-Mark, P.J., Harris, A.J.L., Rowland, S.K., 2007. Terrestrial analogs to the calderas of the tharsis volcanoes on Mars. In: Chapman, M. (Ed.), The Geology of Mars: Evidence from Earth-Based Analogs. Cambridge University Press, Cambridge, UK, pp. 71–94.

Oppenheimer, C., 1991. Lava flow cooling estimated from Landsat Thematic Mapper infrared data: the Lonquimay eruption (Chile, 1989). J. Geophys. Res. 96, 21865–21878.

Osterloo, M.M., Hamilton, V.E., Bandfield, J.L., Glotch, T.D., Baldridge, A.M., Christensen, P.R., Tornabene, L.L., Anderson, F.S., 2008. Chloride-bearing materials in the southern highlands of Mars. Science 319, 1651–1654.

Palluconi, F.D., Kieffer, H.H., 1981. Thermal inertia mapping of Mars from 60 S to 60 N. Icarus 45, 415–426.

Patrick, M.R., 2007. Dynamics of Strombolian ash plumes from thermal video: motion, morphology, and air entrainment. J. Geophys. Res. 112. http://dx.doi.org/10.1029/2006JB004387.

Peet, V.M., Ramsey, M.S., Crown, D.A., 2007. Remote sensing analyses of small terrestrial volcanic and impact craters: a Mars analog for formation, morphology, and erosional processes. Lunar Planetary Science Conference #XXXVIII, abstract #2330.

Pieri, D.C., Baloga, S.M., 1986. Eruption rate, area, and length relationships for some Hawaiian lava flows. J. Volcanol. Geotherm. Res. 30, 29–45.

Platz, T., Michael, G.G., 2011. Eruption history of the Elysium Volcanic Province, Mars. Earth Planet. Sci. Lett. 312, 140–151. http://dx.doi.org/10.1016/j.epsl.2011.10.001.

Plescia, J.B., 2004. Morphometric properties of Martian volcanoes. J. Geophys. Res. 109. http://dx.doi.org/10.1029/2002JE002031.

Prata, A.J., 2009. Satellite detection of hazardous volcanic clouds and the risk to global air traffic. Nat. Hazards 51, 303–324. http://dx.doi.org/10.1007/s11069-008-9273-z.

Prata, A.J., Bernardo, C., 2009. Retrieval of volcanic ash particle size, mass and optical depth from a ground-based thermal infrared camera. J. Volcanol. Geotherm. Res. 186, 91–107. http://dx.doi.org/10.1016/j.jvolgeores.2009.02.007 (ISSN 0377–0273).

Price, J.C., 1977. Thermal inertia mapping: a new view of the earth. J. Geophys. Res. 82, 2582–2590.

Price, M.A., Ramsey, M.S., Crown, D.A., 2013. Thermophysical characteristics of mantled terrestrial volcanic surfaces: infrared analogs to the Arsia Mons flows. Lunar Planetary Science Conference #XLIV, abstract #1640.

Price, M.A., Ramsey, M.S., Crown, D.A., 2016. Thermophysical characteristics of terrestrial volcaniclastic deposits: analog analysis for mantled lava flows on Mars. Remote Sens. (in press).

Putzig, N.E., Mellon, M.T., 2007. Apparent thermal inertia and the surface heterogeneity of Mars. Icarus 191, 68–94.

Ramsey, M.S., 2012. Dynamics of the lava dome at Shiveluch volcano, Kamchatka assessed using near-field remote sensing. Am. Geophys. Union (abstract V34A-04).

Ramsey, M.S., 2015. Synergistic use of satellite thermal detection and science: a decadal perspective using ASTER. In: Harris, A., DeGroeve, T., Garel, F., Carn, S.A. (Eds.), Detecting, Modelling and Responding to Effusive Eruptions 426. Geological Society of London Special Publications.

Ramsey, M.S., Christensen, P.R., 1998. Mineral abundance determination: quantitative deconvolution of thermal emission spectra. J. Geophys. Res. 103, 577–596.

Ramsey, M.S., Crown, D.A., 2010. Thermophysical and spectral variability of Arsia Mons lava flows. Lunar Planetary Science Conference #XLI, abstract #1111.

Ramsey, M.S., Crown, D.A., 2011. Thermophysical properties of mantled volcanic surfaces: can terrestrial analogues be used to better understand Martian volcanism. Am. Geophys. Union (abstract #P42C-06).

Ramsey, M.S., Fink, J.H., 1999. Estimating silicic lava vesicularity with thermal remote sensing: a new technique for volcanic mapping and monitoring. Bull. Volcanol. 61, 32–39.

Ramsey, M.S., Harris, A.J.L., 2013. Volcanology 2020: how will thermal remote sensing of volcanic surface activity evolve over the next decade? J. Volcanol. Geotherm. Res. 249, 217–233.

Ramsey, M.S., Crown, D.A., Price, M.A., 2012a. Decoupling lava flow composition and emplacement processes from eolian mantling deposits using thermal infrared data. Lunar and Planetary Science Conference #XLIII, abstract #2013.

Ramsey, M.S., Wessels, R.L., Anderson, S.W., 2012b. Surface textures and dynamics of the 2005 lava dome at Shiveluch Volcano, Kamchatka. Geol. Soc. Am. Bull. 124. http://dx.doi.org/10.1130/B30580.1.

Rhéty, M., 2014. Down-Channel Cooling and Crystallization of Lava during a Short-Lived Eruption (MSc Thesis) Laboratoire Magmas et Volcans, Clermont Ferrand, France (26 p).

Rieder, R., Economou, T., Wänke, H., Turkevich, A., Crisp, J., Brückner, J., McSween, H.Y., 1997. The chemical composition of Martian soil and rocks returned by the mobile alpha proton X-ray spectrometer: preliminary results from the X-ray mode. Science 278, 1771–1774.

Robert, B., Harris, A., Gurioli, L., Médard, E., Sehlke, A., Whittington, A., 2014. Textural and rheological evolution of basalt flowing down a lava channel. Bull. Volcanol. 76, 1–21. http://dx.doi.org/10.1007/s00445-014-0824-8.

Rogers, A.D., Aharonson, O., 2008. Mineralogical composition of sands in Meridiani Planum determined from Mars Exploration Rover data and comparison to orbital measurements. J. Geophys. Res. 113 http://dx.doi.org/10.1029/2007JE002995.

Rogers, A.D., Christensen, P.R., 2007. Surface mineralogy of Martian low-albedo regions from MGS-TES data: implications for upper crustal evolution and surface alteration. J. Geophys. Res. 112. http://dx.doi.org/10.1029/2006JE002727.

Rogers, A.D., Hamilton, V.E., 2015. Compositional provinces of Mars from statistical analyses of TES, GRS, OMEGA and CRISM data. J. Geophys. Res. 120, 62–91.

Rogers, A.D., Bandfield, J.L., Christensen, P.R., 2007. Global spectral classification of Martian low-albedo regions with Mars Global Surveyor Thermal Emission Spectrometer (MGS-TES) data. J. Geophys. Res. 112. http://dx.doi.org/10.1029/2006JE002726.

Rosema, A., Fiselier, J., 1990. Meteosat-based evapotranspiration and thermal inertia mapping for monitoring transgression in the Lake Chad region and Niger Delta. Int. J. Remote Sens. 11, 741–752.

Rothery, D.A., Francis, P.W., Wood, C.A., 1988. Volcano monitoring using short wavelength infrared data from satellites. J. Geophys. Res. 93, 7993–8008.

Rowland, S.K., Harris, A.J.L., Garbeil, H., 2004. Effects of Martian conditions on numerically modeled, cooling-limited, channelized lava flows. J. Geophys. Res. 109. http://dx.doi.org/10.1029/2004JE002288.

Ruff, S.W., Niles, P.B., Alfano, F., Clarke, A.B., 2014. Evidence for a Noachian-aged ephemeral lake in Gusev crater, Mars. Geology 42, 359–362.

Salisbury, J.W., D'Aria, D.M., 1992. Emissivity of terrestrial materials in the 8–14 μm atmospheric window. Remote Sens. Environ. 42, 83–106.

Salisbury, J.W., Walter, L.S., 1989. Thermal infrared (2.5–13.5 μm) spectroscopic remote sensing of igneous rock types on particulate planetary surfaces. J. Geophys. Res. 94, 9192–9202.

Scheidt, S., Ramsey, M.S., Lancaster, N., 2010. Determining soil moisture and sediment availability at White Sands Dune Field, NM from apparent thermal inertia (ATI) data. J. Geophys. Res. 115. http://dx.doi.org/10.1029/2009JF001378.

Scott, D.H., Tanaka, K.L., 1982. Ignimbrites of the Amazonis Planitia region of Mars. J. Geophys. Res. 87, 1179–1190.

Simurda, C.M., Ramsey, M.S., Crown, D.A., 2015. Thermophysical characteristics of lava flows south of Arsia Mons. Lunar Planetary Science Conference #XLVI, abstract #2332.

Skilling, I.P., 2002. Basaltic pahoehoe lava-fed deltas: large-scale characteristics, clast generation, emplacement processes and environmental discrimination. In: Smellie, J.L., Chapman, M.G. (Eds.), Volcano-Ice Interaction on Earth and Mars. Geological Society Special Publication 202, pp. 91–114.

Smith, M.D., Pearl, J.C., Conrath, B.J., Christensen, P.R., 2000. Mars global surveyor thermal emission spectrometer (TES) observations of dust opacity during aerobraking and science phasing. J. Geophys. Res. 105, 9539–9552.

Tanaka, K.L., Skinner, J.A., Dohm, J.M., Irwin, R.P., Kolb, E.J., Fortezzo, C.M., Platz, T., Michael, G.G., Hare, T.M., 2014. Geologic map of Mars. United States Geological Survey Scientific Investigations Series Map 3292, scale 1:20 M.

Thomson, J.L., Salisbury, J.W., 1993. The mid-infrared reflectance of mineral mixtures (7–14 μm). Remote Sens. Environ. 45, 1–13.

Tramutoli, V., 1998. Robust AVHRR techniques (RAT) for environmental monitoring: theory and applications. In: Cecchi, G., Zilioli, E. (Eds.), Earth Surface Remote Sensing II: Proceedings of SPIE. 3496, pp. 101–113.

Turcotte, D.L., Schubert, G., 2002. Geodynamics. second ed. Cambridge University Press, Cambridge, UK (456 pp. ISBN: 978–0-521-66624-4).

Vaughan, R.G., Hook, S.J., Ramsey, M.S., Realmuto, V.J., Schneider, D.G., 2005. Monitoring eruptive activity at Mount St. Helens with TIR image data. Geophys. Res. Lett. 32, L19305. http://dx.doi.org/10.1029/2005GL024112.

Vicari, A., Ciraudo, A., Del Negro, C., Herault, A., Fortuna, L., 2009. Lava flow simulations using discharge rates from thermal infrared satellite imagery during the 2006 Etna eruption. Nat. Hazards 50, 539–550. http://dx.doi.org/10.1007/s11069-008-9306-7.

Vicari, A., Ganci, G., Behncke, B., Cappello, A., Neri, M., Del Negro, C., 2011. Near-realtime forecasting of lava flow hazards during the 12–13 January 2011 Etna eruption. Geophys. Res. Lett. 38 (13). http://dx.doi.org/10.1029/2011GL047545.

Villeneuve, N., Neuville, D.R., Boivin, P., Bachèlery, P., Richet, P., 2008. Magma crystallization and viscosity: a study of molten basalts from the piton de la fournaise volcano (La Réunion island). Chem. Geol. 256, 242–251.

Watson, I.M., Realmuto, V.J., Rose, W.I., Prata, A.J., Bluth, G.J.S., Gu, Y., Bader, C.E., Yu, T., 2004. Thermal infrared remote sensing of volcanic emissions using the moderate resolution imaging spectroradiometer. J. Volcanol. Geotherm. Res. 135, 75–89.

Werner, S.C., 2005. Major aspects of the chronostratigraphy and geologic evolutionary history of Mars. Ph.D. Dissertation, Freien Universitat Berlin, p. 160.

Wilson, L., Head, J.W., 1994. Mars: review and analysis of volcanic eruption theory and relationships to observed landforms. Rev. Geophys. 32, 221–263.

Wilson, L., Mouginis-Mark, P.J., 2001. Estimation of volcanic eruption conditions for a large flank event on Elysium Mons, Mars. J. Geophys. Res. 106, 20621–20628.

Wright, R., Blake, S., Harris, A., Rothery, D., 2001. A simple explanation for the space-based calculation of lava eruptions rates. Earth Planet. Sci. Lett. 192, 223–233.

Wright, R., Flynn, L.P., Garbeil, H., Harris, A.J.L., Pilger, E., 2004. MODVOLC: near-realtime thermal monitoring of global volcanism. J. Volcanol. Geotherm. Res. 135, 29–49. http://dx.doi.org/10.1016/j.jvolgeores.2003.12.008 (ISSN 0377–0273).

Wright, R., Carn, S.A., Flynn, L.P., 2005. A satellite chronology of the May–June 2003 eruption of Anatahan volcano. J. Volcanol. Geotherm. Res. 146, 102–116.

Wright, R., Garbeil, H., Harris, A.J.L., 2008. Using infrared satellite data to drive a thermo-rheological/stochastic lava flow emplacement model: a method for near real-time volcanic hazard assessment. Geophys. Res. Lett. 35 http://dx.doi.org/10.1029/2008GL035228.

Wyatt, M.B., McSween, H.Y., 2002. Spectral evidence for weathered basalt as an alternative to andesite in the northern lowlands of Mars. Nature 417 (6886), 263–266.

Zimbelman, J.R., Garry, W.B., Bleacher, J.E., Crown, D.A., 2015. Volcanism on Mars. In: Sigurdsson, H., Houghton, B., Rymer, H., Stix, J., McNutt, S. (Eds.), The Encyclopedia of Volcanoes, second ed. Academic Press, New York, pp. 717–728.